JOURNAL OF PETROLOGY | VOLUME 0 | NUMBER 0 | PAGES 1–32 | 2012 | doi:10.1093/petrology/egs017

Journal of Petrology Advance Access published April 11, 2012

Hornblende Chemistry in Meta- and Diatexites and its Retention in the Source of Leucogranites: an Example from the Karakoram Shear Zone, NW India

HENNING REICHARDT* AND ROBERTO F. WEINBERG

SCHOOL OF GEOSCIENCES, MONASH UNIVERSITY, CLAYTON, VIC. 3800, AUSTRALIA

RECEIVED JULY 1, 2010; ACCEPTED FEBRUARY 10, 2012

A suite of calc-alkaline arc rocks in the Pangong Metamorphic Complex in the Karakoram Shear Zone, Ladakh, NW India, was migmatized at upper amphibolite facies under water-fluxed conditions. Meta- and diatexites contain abundant hornblende in both leucosome and melanosome. These form idiomorphic, poikilitic megacrysts in the leucosome and in melanosome rims around leucosomes. Hornblende chemistry, particularly its rare earth element (REE) pattern, is highly variable in protoliths and neosomes, and in most cases the REE contents do not reflect hornblende partition coefficients reported in the literature. These variations are the result of the complex crystallization histories of the migmatites. REE variations in whole-rock diatexites and leucogranites demonstrate the role of hornblende in controlling the REE budget. Formation of heavy REE (HREE)-enriched hornblende and its accumulation in the source results in leucogranitic magmas with high La_n/Yb_n and Sr/Y values typical of adakites. We show that leucogranitic magmas, depleted in HREE, can be generated by water-fluxed partial melting of arc-related rocks in the mid-crust without requiring garnet retention in the source.

KEY WORDS: *magma; migmatite; hornblende; REE*

INTRODUCTION

Fractionation of hornblende is a significant factor in crustal differentiation (Arth & Barker, 1976; Defant & Drummond, 1990; Patiño Douce, 1999; Foley *et al.*, 2002; Davidson *et al.*, 2007). The geochemical signatures of Archean tonalite–trondhjemite–granodiorites (TTGs) and adakites, with typical high La_n/Yb_n and Sr/Y values, are generally thought to be largely the result of fractionation processes that create residual assemblages rich in hornblende and garnet in the source (Martin, 1987, 1999; Defant & Drummond, 1990; Nehring *et al.*, 2009). TTGs are generally regarded as the products of partial melting of basaltic crustal rocks under high pressure in the stability field of garnet, probably during subduction of oceanic crust or at the base of thickened continental crust; this melting process leaves garnet-amphibolite or eclogite as a residue (Drummond & Defant, 1990; Martin, 1994). Examples of high La_n/Yb_n and Sr/Y signatures in Phanerozoic plutonic belts, such as the Cordillera Blanca Batholith in Peru and the Separation Point suite of the Median Batholith in New Zealand, have been proposed to be the result of deep melting of a mafic crustal underplate within the garnet stability field that also produces a hornblende- and garnet- bearing residue (Petford & Atherton, 1996; Tulloch & Kimbrough, 2003). Tiepolo & Tribuzio (2008), however, have proposed that hornblende fractionation alone, without involvement of garnet, can account for highly fractionated, heavy rare earth element (HREE)-depleted magmas. Although many model calculations are well constrained in terms of whole-rock and mineral chemistry, field relations that confirm the modelled processes are relatively scarce because they involve mantle and lower crustal restitic rocks or melt sources that are rarely exposed.

The Pangong Metamorphic Complex in Ladakh, NW India, exposes migmatites that have hornblende as a

*Corresponding author. E-mail: Henning.Reichardt@monash.edu

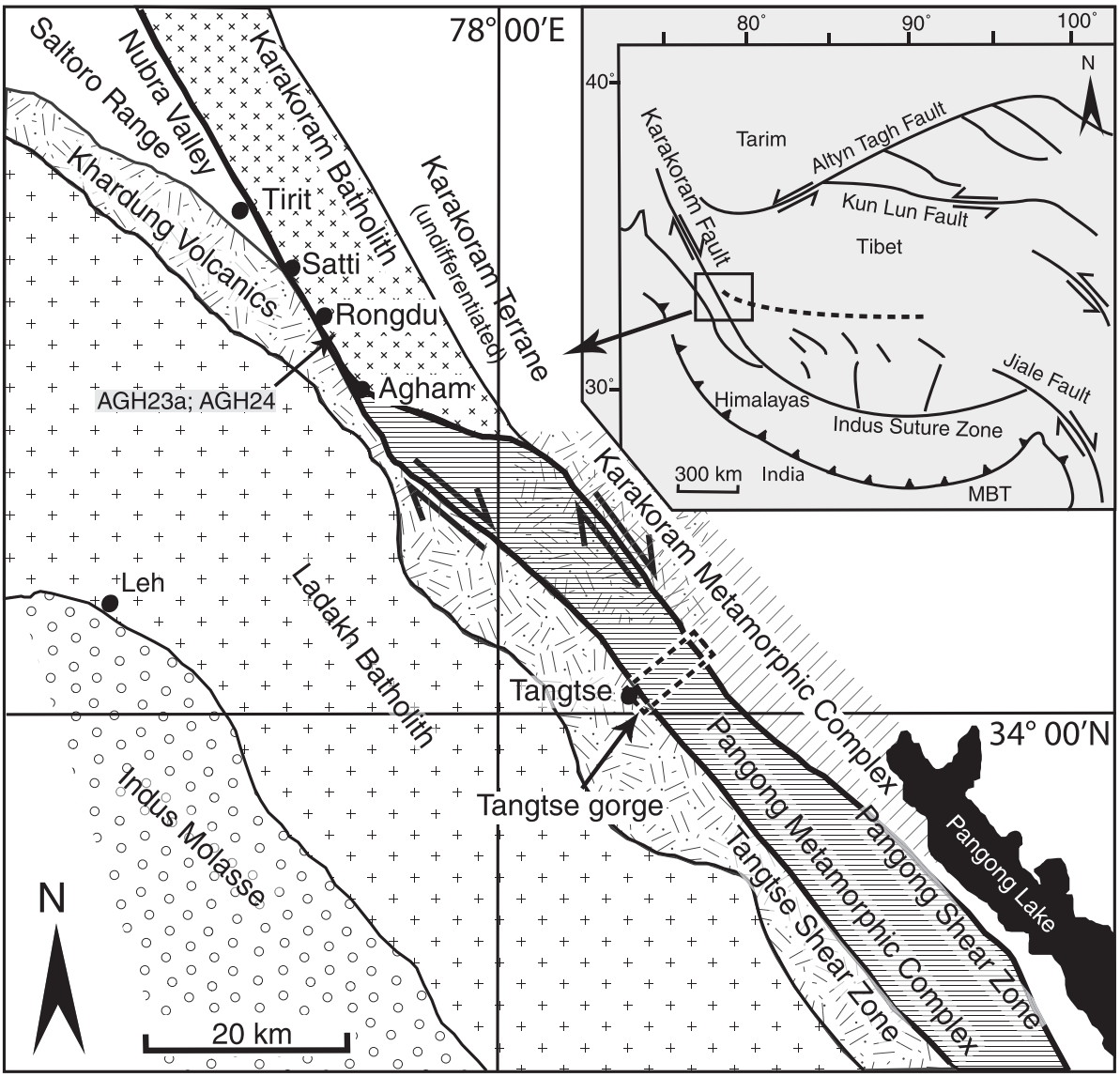

Fig. 1. Geological map of the Karakoram Shear Zone in Ladakh, NW India. Location of the Tangtse gorge in the Pangong Metamorphic Complex (PMC) is indicated by dashed rectangle. Sample location in the Rongdu area is indicated by arrow. MBT, Main Boundary Thrust.

peritectic phase. *In situ* leucosomes feed into a network of leucogranite magma sheets that locally coalesce to form stocks and plutons, and eventually feed into the Karakoram Batholith (Reichardt *et al.*, 2010; Reichardt & Weinberg, 2012). Building on the observed field relations, here we investigate hornblende chemistry and its link with the REE composition of the source rocks, meta- and diatexites, and leucogranites. We show that hornblende REE patterns vary between samples and that hornblende fractionation exerts a strong control on the REE budget of the daughter magmatic rocks, explaining why some of these rocks have high La_n/Yb_n and Sr/Y values similar to Archean TTGs and adakites.

GEOLOGICAL BACKGROUND

The Pangong Metamorphic Complex is exposed in the central part of the Karakoram Shear Zone (Fig. 1). Here, the shear zone that trends NW–SE for at least 700 km from the Pamir Mountains in Pakistan through the Eastern Karakoram to the Mt Kailas region in India, is divided into two parallel strands, the Tangtse and the Pangong Shear Zones (Fig. 1). The Tangtse Shear Zone separates rocks of the Ladakh arc to the SW from those of the Pangong Metamorphic Complex (PMC). The Pangong Shear Zone separates the PMC from the rocks of the Karakoram Metamorphic Complex (KMC) to the

NE. The Ladakh arc comprises mainly calc-alkaline granitoids, ranging from granites to gabbros, which have crystallization ages ranging between 49 and 103 Ma, and are associated with a volcanic sequence, known as the Khardung Volcanics (Schärer *et al.*, 1984; Weinberg & Dunlap, 2000; Singh *et al.*, 2007; Upadhyay *et al.*, 2008). The KMC consists mainly of staurolite–garnet schists, amphibolites and marbles (McCarthy & Weinberg, 2010). The PMC comprises a calc-alkaline granitoid suite of Hbl–Bt-granodiorites and diorites, consisting of varying proportions of plagioclase, K-feldspar, quartz, hornblende and titanite, commonly with the accessory minerals allanite, apatite and zircon. Mineral abbreviations are after Kretz (1983). Mafic varieties of the diorites commonly contain clinopyroxene. Only the Bt-granodiorites are hornblende-free. This calc-alkaline suite forms the Muglib Batholith (Weinberg *et al.*, 2009; Reichardt *et al.*, 2010) and intrudes amphibolites, calc-silicate rocks, Bt-psammites, Bt-pelites and minor marble beds. Rocks of the Muglib Batholith have crystallization ages centred around 70 Ma (Weinberg *et al.*, 2000; Ravikant, 2006; Reichardt *et al.*, 2010) and isotopic compositions similar to those of the Ladakh arc (Ravikant, 2006; Reichardt *et al.*, 2010). Amphibolites in the PMC have been related to volcanic rocks of the Ladakh arc (Rolland *et al.*, 2002, 2009). The whole-rock geochemistry of all major rock groups in the PMC, which show the typical calc-alkaline trends of arc-related volcanic rocks, has been discussed by Reichardt *et al.* (2010).

Rolland & Pêcher (2001) determined that peak metamorphic temperatures in the Tangtse area reached $700 \pm 20^{\circ}C$ at 7 ± 1 kbar, based on the association of muscovite and sillimanite in the absence of K-feldspar in metapelites and cation exchange reactions (minerals used: Grt–Bt, Grt–Pl–Ms–Qtz, Grt–Pl–Ms–Bt and Grt–Pl–Sil–Qtz). Rocks of the calc-alkaline granitoid suite and the Bt-psammites are both migmatized (Reichardt *et al.*, 2010), and the leucosomes are physically linked to leucogranite dykes, stocks and plutons that span crystallization ages from ~13·5 to ~20 Ma (Searle *et al.*, 1998; Weinberg & Searle, 1998; Phillips *et al.*, 2004; Ravikant *et al.*, 2009; Reichardt *et al.*, 2010) and have been related to anatexis of the PMC, based on field relations, geochronological and isotopic data (Weinberg & Searle, 1998; Reichardt *et al.*, 2010). These leucogranite dykes and sheets link the source region to the Karakoram Batholith, and are generally mildly peraluminous Bt ± Ms ± Grt-leucogranites to leucotonalites and commonly record evidence of feldspar accumulation such as high Sr and Ba (Reichardt *et al.*, 2010).

This study focuses on exposures in the Tangtse gorge (Fig. 1), which transects the Karakoram Shear Zone and exposes a cross-section of all the major lithologies in the PMC, including a several hundred meter-wide layer of meta- and diatexites and the Pangong Injection Complex (Weinberg & Searle, 1998; Weinberg *et al.*, 2009).

MIGMATITE MORPHOLOGY AND HORNBLENDE ACCUMULATION

In the Tangtse gorge area (Fig. 2) migmatized calc-alkaline magmatic rocks contain abundant hornblende in the leucosome. Metatexites exhibit alternating leucocratic, mesocratic and melanocratic layers. These are interpreted to represent melt-enriched parts (leucosome) and melt-depleted, residual parts (melanosome), as well as compositional differences in the unmelted protolith. Mesocratic layers (mesosome) in migmatized areas are also regarded as melanosome because they are inferred to have lost melt.

Leucosomes have varying modal contents of plagioclase, K-feldspar, quartz, hornblende, biotite and titanite giving rise to compositional variations from leucogranite to trondhjemite. They are mostly medium-grained, but plagioclase and K-feldspar megacrysts up to ~3 cm long are common. Tonalitic leucosomes are generally physically associated with more mafic, dioritic protoliths. The leucosomes commonly have dextral C–S fabrics defined by deformed and asymmetric feldspar, and biotite foliae wrapping around feldspar grains. Leucosomes with diffuse boundaries to melanosome in shear planes suggest syn-deformational melting. Tight to isoclinal folds that have leucosomes parallel to the axial plane that are continuous with layer-parallel leucosomes further indicate that melting and deformation were coeval (Weinberg & Mark, 2008). Continuous folding and shearing of leucosome-bearing layers has led to disaggregation of the metatexites to form diatexites (Fig. 2a and b; see also Weinberg & Mark, 2008). Disaggregation of layering also gives rise to schlieren consisting mostly of hornblende, biotite and titanite (Fig. 2c). Amphibolite blocks that seem unaffected by anatexis form schollen in the diatexite (Fig. 2d). Here, the term schollen describes rafts of non-leucosome in leucosome (Mehnert, 1968). In some examples, these blocks, which can be up to ~1·5 m across, are internally fragmented but are still recognizable as one formerly coherent block (Fig. 2e). There are also large areas where the protolith magmatic rocks are not migmatized, presumably because of the absence of infiltrating fluid.

Commonly, hornblende in the leucosomes forms large crystals (up to 3 cm), which are poikilitic and euhedral (Fig. 2f). In many places, the diatexites have a patchy texture characterized by leucosome grading into melanosome (Fig. 3a). Locally, patchy leucosomes contain hornblende-rich areas (Fig. 3c). Leucosomes in quartz-diorites also contain aggregates of hornblende (Fig. 3d). Isolated rafts of mafic diorite in leucosome are commonly rimmed by hornblende megacrysts. In some locations, dark veins

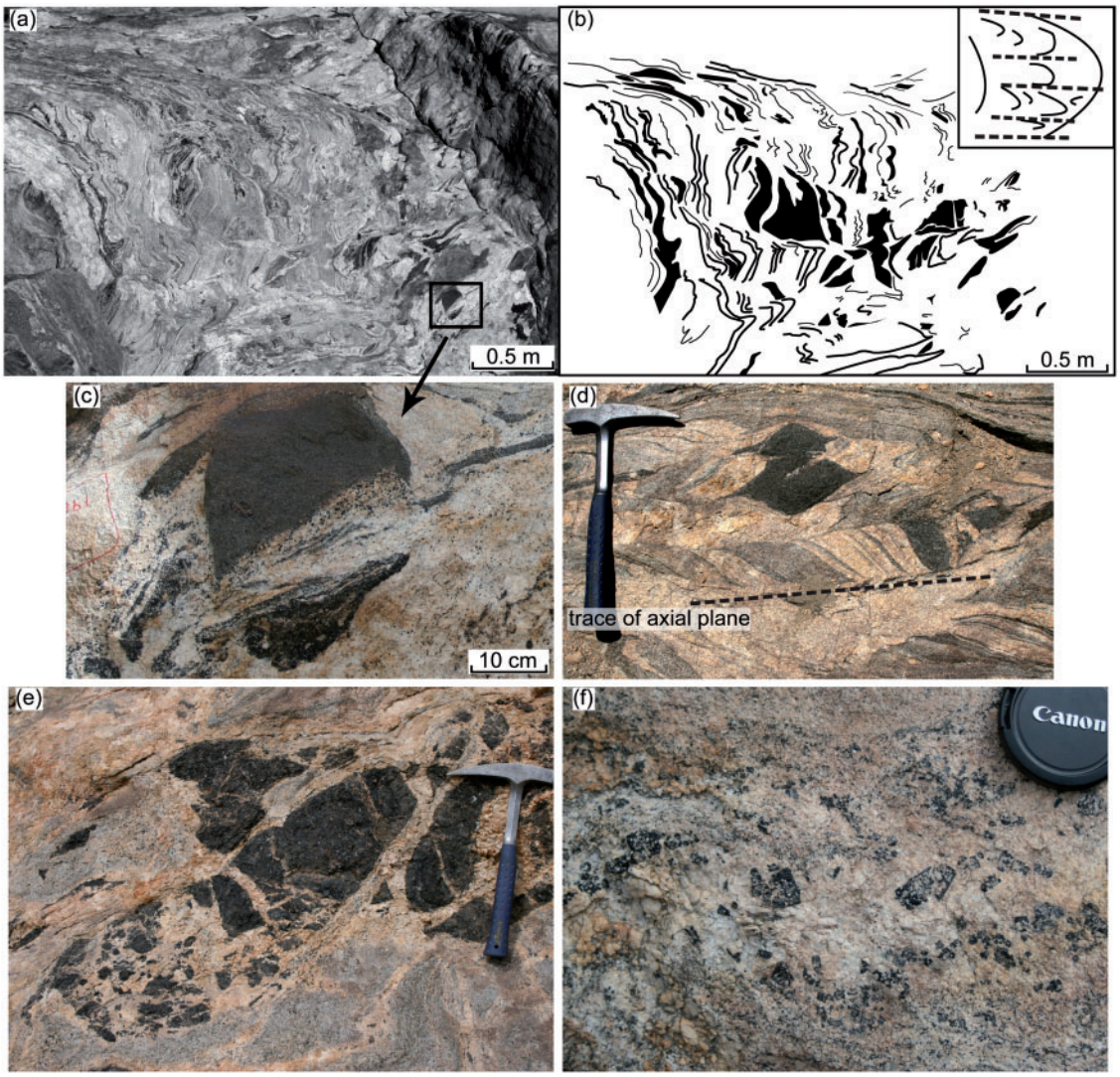

Fig. 2. General features of hornblende-bearing migmatites in the Tangtse gorge. (a) Disaggregation of metatexite to form diatexite. The outcrop is~20° inclined towards viewer. (b) Line drawing of (a) showing folding of layers. Inset: interpretation of folding and axial planar leucosomes indicated as dashed lines. (c) Disrupted amphibolite schollen and entrainment of schollen material to form schlieren in leucosome. (d) Rotation of layering in metatexite into parallelism with axial plane. (e) Fragmented amphibolite schollen in diatexite migmatite. Fragments are surrounded by leucosome but show jigsaw fit. (f) Large, euhedral poikilitic hornblende megacrysts in leucosome in Hbl–Bt-granodiorite.

consist mostly of hornblende (Fig. 3e). These ~5–10 cm thick veins are continuously linked to wider (~0·5 m) leucosomes and are interpreted as parts of the leucosome from which the interstitial melt has been extracted, leaving behind an accumulation of early formed crystals. Hornblende is interpreted to be a peritectic product of the melting reaction because of its poikilitic and porphyritic habit in the leucosomes, and because it forms melanosome rims around leucosomes.

PETROGRAPHY

Under the microscope the typical hornblende is dark green and lacks visible zonation. Samples from the Rongdu area (Fig. 1) are an exception and contain hornblende grains with patchy zoning or with green–brown cores and green rims. Hornblende is petrographically distinct in protolith, melanosome and leucosome. In granodiorite and quartz-diorite protoliths, hornblende is subhedral to anhedral, rarely exceeds 5 mm in length, and is generally aligned with the regional tectonic fabric (Fig. 4a); in places it has a sigmoidal shape. Hornblende in leucosomes, patchy melanosomes and melanosome rims around leucosomes is significantly larger than that in the protoliths, ranging from a few millimetres to megacrysts up to ~3 cm long. Grains are euhedral to subhedral, poikilitic and commonly have inclusions of plagioclase, K-feldspar, biotite, allanite and apatite (Fig. 4b). Locally developed patchy tonalitic

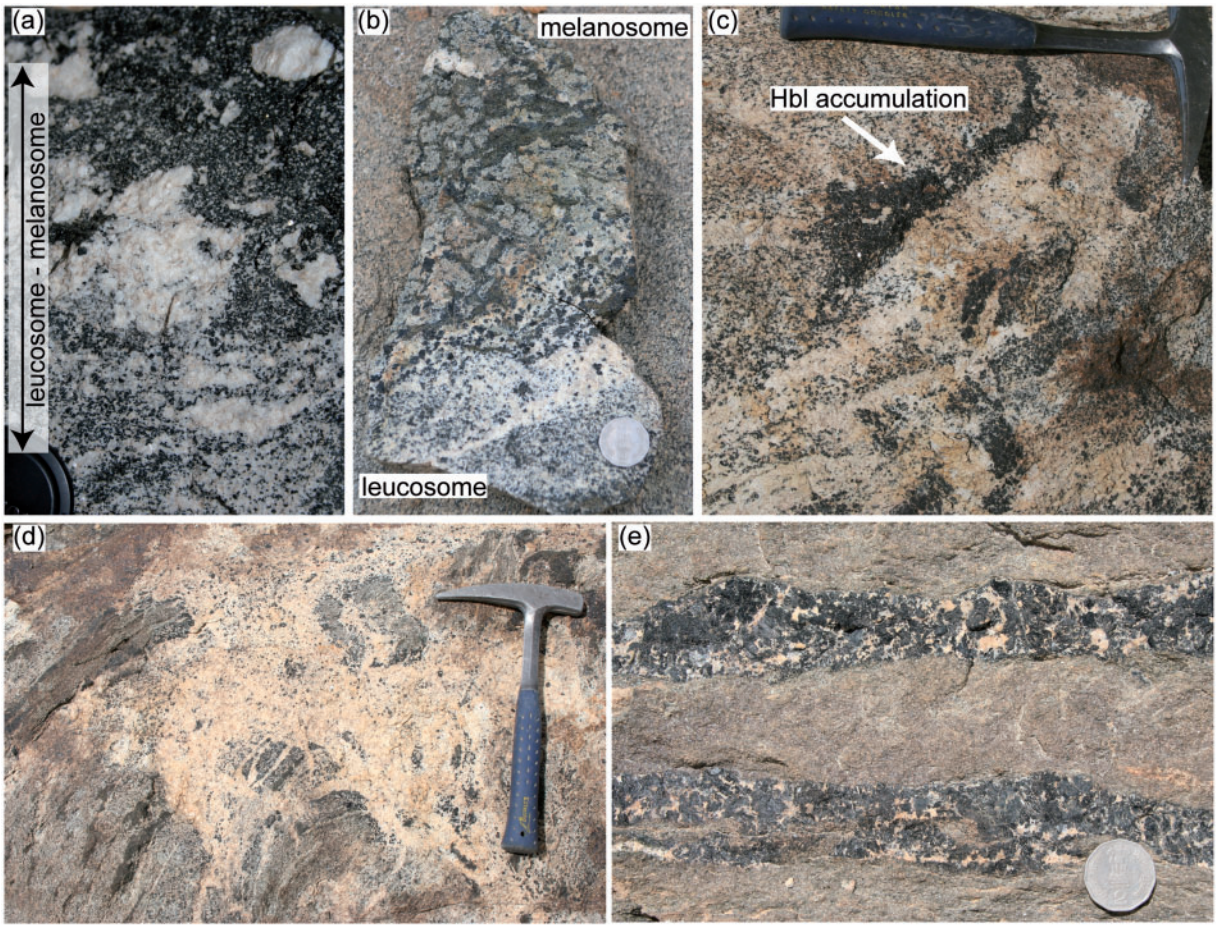

Fig. 3. (a) Grading from melanosome into leucosome in diatexite; diorite protolith. (b) Mottled texture formed by clinopyroxene clusters (pale green) surrounded by hornblende (dark green) and biotite in melanosome of metatexite. Diffuse, patchy leucosome consisting mostly of hornblende and K-feldspar. Protolith is diorite. (c) Hornblende accumulation in Hbl–Bt-granodiorite. (d) Patchy, coarse-grained Hbl-bearing leucosome in diorite. Schollen of diorite (e.g. at tip of hammer) show rims of hornblende megacrysts. (e) Hornblende and K-feldspar accumulation in veins in diorite, interpreted to be the result of melt extraction from a leucosome that now preserves a residual assemblage.

leucosomes have a hypidiomorphic magmatic texture with euhedral to subhedral hornblende megacrysts that have plagioclase inclusions (Fig. 4c). Here, plagioclase is usually euhedral, whereas quartz is present in the interstices (Fig. 4d). Compared with hornblende in the paleosome, hornblende in the leucosomes is generally not aligned.

In the diatexites, hornblende grains in leucocratic parts show two different habits: one is characterized by euhedral to subhedral poikilitic grains, whereas the other is anhedral and generally smaller and has higher aspect ratios. Grains with the latter texture also occur in schlieren together with biotite and titanite and are commonly physically linked to a melanosome. Where the premigmatization texture is still preserved in outcrops of Hbl–Bt-granodiorite, thin rims of felsic material of unknown composition are found around the plagioclase and K-feldspar grains. Sometimes, these films connect interstices between larger, framework building plagioclase and K-feldspar grains (Fig. 4e). Small embayed plagioclase grains are also common. These features indicate either low degrees of partial melting or crystallization of small amounts of residual melt after melt extraction (Fig. 4e; Sawyer, 1999, 2001).

Some leucosomes in the Hbl–Bt-granodiorites and diorites contain only K-feldspar, quartz and hornblende as major minerals. Plagioclase is present only in interstices, as thin rims around hornblende and K-feldspar, or as inclusions in hornblende. These leucosomes also contain significant amounts of apatite and titanite (Fig. 4f), small, commonly anhedral clinopyroxene grains, and allanite. In these leucosomes, hornblende grains contain exceptionally large amounts of euhedral apatite inclusions (Fig. 4b). Allanite grains in patchy melanosomes around these Hbl–Kfs leucosomes are commonly larger than 500 μm, and

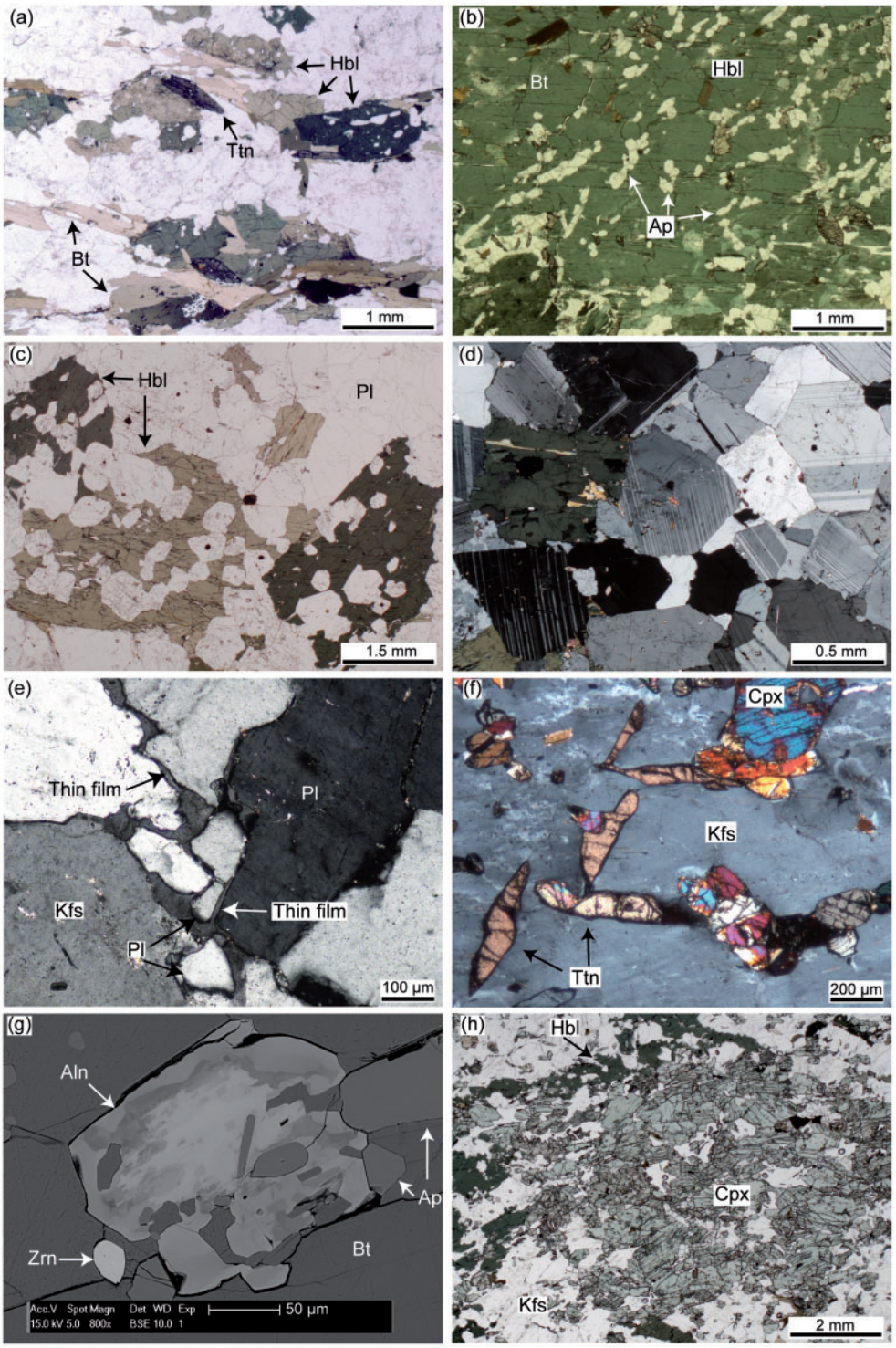

Fig. 4. Photomicrographs. (a) Example of hornblende texture in calc-alkaline Hbl–Bt-granodiorite protolith. Hornblende is mostly subhedral to anhedral and aligned together with biotite and titanite forming the foliation. Plane-polarized light (PPL). (b) Large amounts of euhedral apatite inclusions in hornblende megacryst in Hbl–Kfs leucosome in rocks such as shown in Fig. 3c. PPL. (c) Euhedral, poikilitic hornblende megacrysts with mainly plagioclase, but also quartz inclusions in tonalitic leucosome (PPL); diorite protolith. (d) Same leucosome as in (c), showing granoblastic texture and straight boundaries between plagioclase grains (XPL). (e) Thin film between grains in Hbl–Bt-granodiorite. Small plagioclase grains in centre of image are interpreted to have undergone melting. This interpretation is based on embayment of plagioclase grains, for example on the small Pl grain in the lower centre that is enclosed by the film. Cross-polarized light (XPL). (f) Titanite and clinopyroxene in Hbl–Kfs leucosome. Most of the field of view is taken up by K-feldspar. Some of the titanite grains fill interstitial space between K-feldspar grains (e.g. in upper, central part of image); most clinopyroxene grains are small, anhedral and enclosed by K-feldspar (XPL); diorite protolith. (g) Scanning electron microscope image showing zoned allanite with apatite inclusions, apatite and zircon in biotite schlieren in migmatitic calc-alkaline Bt-granodiorite. (h) Cluster of subhedral, and small (<500 μm) anhedral clinopyroxene grains in a patchy melanosome of mottled diorite as shown in Fig. 3b (PPL).

allanite is also common in biotite schlieren in migmatitic Bt-granodiorite (Fig. 4g). Locally, Hbl–Kfs leucosomes in quartz-diorite grade into melanosome, characterized by dark green rims of hornblende ± biotite surrounding pale green clusters of clinopyroxene giving rise to a mottled texture (Figs 3b and 4h).

Anatectic products lack anhydrous minerals, such as orthopyroxene or garnet, expected from dehydration melting reactions. Melting experiments have demonstrated that hornblende is stable as a crystallizing phase concomitant with melt production only when external water is added (Gardien *et al.*, 2000). Based on the thermobarometric constraints ($T = 700 \pm 20^{\circ}C$, $P = 7 \pm 1$ kbar; Rolland & Pêcher, 2001) and petrography, especially the widespread occurrence of hornblende in the leucosomes and their melanocratic rims, we infer that migmatization took place under water-fluxed conditions (Weinberg & Mark, 2008; Reichardt *et al.*, 2010). We suggest the following melt-producing reactions that have been documented in migmatites with comparable mineral assemblages (Lappin & Hollister, 1980; McLellan, 1988):

$$\text{Bt} + \text{Pl} + \text{Qtz} + \text{H}_2\text{O-rich fluid} \rightarrow \text{Hbl} + \text{melt}$$

or

$$\text{Bt} + \text{Pl} + \text{Qtz} + \text{H}_2\text{O-rich fluid} \rightarrow \text{Hbl} + \text{Kfs} + \text{melt}.$$

Abundant small, often euhedral titanite in the Hbl–Kfs leucosomes (Fig. 4f) suggests a third melt-producing reaction (Lappin & Hollister, 1980):

$$\text{Bt} + \text{Pl(I)} + \text{Qtz} + \text{H}_2\text{O-rich fluid} \rightarrow \text{Hbl} + \text{Pl(II)} + \text{Ttn} + \text{melt}.$$

Because K-feldspar is present in the protolith, the following melting reaction at the wet granite solidus is also inferred to have taken place (Holtz *et al.*, 1992):

$$\text{Pl} + \text{Kfs} + \text{Qtz} + \text{H}_2\text{O-rich fluid} \rightarrow \text{melt}.$$

To constrain the petrogenetic relationships, we have analysed the compositions of representative inferred protoliths, various parts of the migmatites ranging from leucosome to melanosome, and also the leucogranite plutons in the PMC. The results are presented below.

GEOCHEMISTRY

Analytical procedures

Whole-rock analysis

Pulverized whole-rock samples were analysed for major and trace element concentrations after preparation of fused discs and pressed pellets, respectively. Analyses were carried out using a Bruker-AXS S4 Pioneer X-ray fluorescence (XRF) spectrometer at the Advanced Analytical Centre (AAC) of James Cook University. Trace elements in samples labelled with an asterisk in Table 1 were analyzed using a Thermo Finnigan X series II, quadrupole inductively coupled plasma mass spectrometry (ICP-MS) system at Monash University. All Zr values reported are by XRF analysis, except for samples TNG169a and TNG207, for which Zr data are by ICP-MS analysis. Sample solutions were produced from ~50 mg of sample powder using high-pressure digestion methods. ICP-MS count rates were externally standardized by means of calibration curves based on the USGS standard reference materials AGV-1 and RGM-1 following Eggins *et al.* (1997). Drift corrections were applied by the combined use of In and Bi as internal standards and the repeated analysis of dummy standards during the analytical session.

Reproducibility on replicate analyses and external accuracy were of the order of 5% for all elements. Trace element values marked with a dagger in Table 1 were determined by instrumental neutron activation analysis (INAA) of pressed whole-rock powder pellets, performed at Activation Laboratories Ltd., Ontario, Canada.

Mineral analysis

Major element concentrations of minerals were determined by electron microprobe analysis, performed on polished carbon-coated thin sections at The University of Melbourne, School of Earth Sciences. A Cameca SX-50 electron microprobe with four vertical wavelength-dispersive spectrometers (WDS) was used with the following operation conditions: beam current 35 nA, acceleration voltage 15 kV, take-off angle 40°. Detection limits for all elements were better than 0·05 wt % except for Zn, for which the detection limit was 0·09 wt %.

Trace element concentrations were determined via laser ablation (LA)-ICP-MS on polished thick sections (~150 μm). The data were obtained using a New Wave UP 213 nm N:YAG laser ablation microprobe coupled with a Thermo Finnigan X Series II, quadrupole ICP-MS system at Monash University, School of Geosciences. Analyses employed a pulse rate of 4 Hz and beam energy of ~12 J cm^{-2} at the sample. Laser spot size was ~110 μm diameter. For each analysis background readings with the laser switched off were collected for 25 s followed by a 60 s ablation time. The LA-ICP-MS raw data were reduced using the GLITTER 4.0 software package (van Achterbergh *et al.*, 2001). Quantitative results for trace elements were obtained through calibration of relative element sensitivities using the NIST612 glass as an external standard. Electron microprobe data for Ca were used for internal standardization. To improve accuracy, the trace element concentrations were subsequently corrected to the difference between the measured and recommended values of the USGS glass standard AGV1 (see Supplementary Data Appendix 1, available for downloading at http://www.petrology.oxfordjournals.org).

Table 1: Whole rock major and trace element data

Sample	TNG98a*	TNG131a*	TNG131f*	TNG205a*	TNG205b*	TNG207*	TNG62a*	TNG114a*	TNG205c*	TNG168*
Rock type	Hbl-Bt-g.	Bt-g.	Bt-g.	Diorite	Diorite	Hbl-Bt-g.	Mel.	Mel.	Mel.	Amph.
Major Elements wt%										
SiO_2	66·65	67·50	68·70	54·91	55·02	68·23	55·00	53·70	47·62	47·20
TiO_2	0·68	0·56	0·48	1·37	1·16	0·50	1·29	1·46	1·10	1·74
Al_2O_3	16·84	16·30	16·30	17·56	17·07	15·26	18·20	16·90	15·53	12·02
Fe_2O_3t	3·58	3·49	3·35	8·04	7·51	3·05	7·75	8·80	10·25	11·93
MnO	0·09	0·09	0·09	0·13	0·13	0·07	0·15	0·16	0·18	0·12
MgO	1·63	1·57	1·28	3·01	4·64	1·22	3·83	4·26	8·58	10·95
CaO	3·44	3·16	3·37	5·90	8·22	2·85	5·79	7·18	11·78	10·07
Na_2O	4·62	4·37	4·56	3·81	4·08	3·17	4·28	4·17	2·36	1·97
K_2O	1·92	2·85	1·89	2·97	1·11	4·57	2·79	1·75	1·11	1·29
P_2O_5	0·29	0·22	0·17	0·50	0·33	0·19	0·51	0·37	0·15	0·38
LOI	0·65	0·50	0·45	0·82	0·84	0·75	1·00	1·13	1·35	1·53
Total	100·37	100·62	100·62	99·00	100·08	99·65	100·59	99·85	100·12	99·18
A/CNK	1·06	1·02	1·04	0·87	0·75	0·99	0·88	0·77	0·59	0·52
Mg/(Fe + Mg)	0·47	0·47	0·43	0·43	0·55	0·44	0·49	0·49	0·62	0·65
Trace Elements ppm										
Sc	6	8	6	13	17	6	16	27	31	27
Ti	4067	3953	3518	7373	6505	2121	7788	11689	6514	8420
V	62	92	75	124	146	59	152	332	198	239
Cr	13	71	53	13	15	21	50	41	27	57
Mn	557	893	898	859	862	415	1068*	1794	1107	817
Co	10	9	8	28	29	42	21	41	35	45
Ni	16	66	62	17	26	29	41	92	31	92
Cu	6	13	3	48	84	7	63	74	53	191
Zn	63	82	93	87	76	32	112	119	79	114
Ga	19	13	14	14	10	16	22	14	9	12
Rb	117	206	49	124	26	136	122	71	23	39
Sr	543	439	354	569	551	413	542	628	418	354
Y	15·8	20·1	8·5	24·3	20·5	18·7	27·3	16·9	20·8	21·3
Zr	178	164	146			26	280	137		
Nb	18·0	21·4	23·7	25·5	15·1	15·1	27·4	21·6	8·9	10·4
Ba	280	286	84	540	119	434	334	213	118	197
La	55·87	75·25	11·68	58·46	26·21	58·76	55·98	27·57	14·25	18·93
Ce	99·52	103·75	19·54	107·82	52·17	89·25	111·68	46·37	32·18	45·05
Pr	10·54	9·47	2·28	10·58	5·84	9·75	12·29	5·30	3·93	5·78
Nd	35·28	29·82	7·98	39·55	24·30	30·50	42·77	20·04	18·48	26·84
Sm	5·48	5·12	1·71	6·90	4·95	4·81	7·57	4·21	4·43	6·30
Eu	1·32	1·08	0·39	1·67	1·36	1·16	2·03	1·27	1·24	1·63
Gd	4·27	4·14	1·40	5·76	4·03	3·68	6·35	3·53	3·63	4·91
Tb	0·54	0·62	0·24	0·86	0·67	0·52	0·91	0·56	0·63	0·80
Dy	2·80	3·41	1·41	4·53	3·76	3·13	5·06	3·16	3·67	4·27
Ho	0·51	0·71	0·33	0·84	0·74	0·62	1·00	0·68	0·75	0·79
Er	1·36	1·80	0·95	2·32	1·96	1·62	2·69	1·68	1·95	1·97
Tm	0·19	0·24	0·14	0·34	0·30	0·26	0·40	0·21	0·30	0·28
Yb	1·15	1·62	1·14	2·06	1·88	1·68	2·55	1·39	1·87	1·65
Lu	0·16	0·25	0·21	0·32	0·30	20·86	0·37	0·21	0·28	0·24
Pb	10·86	42·98	37·13	12·16	11·45	0·24	11·55	11·00	5·27	3·85
Th	10·60	17·67	5·14	11·21	4·15	17·14	10·93	2·02	1·74	2·06
U	2·32	3·84	2·76	1·08	1·26	2·75	2·84	1·23	1·20	0·80
La_n/Yb_N	32·7	31·3	6·9	19·2	9·4	23·5	14·8	13·3	5·1	7·7
Dy_n/Yb_n	1·6	1·4	0·8	1·4	1·3	1·2	1·3	1·5	1·3	1·7
Sum REE	219·0	237·3	49·4	242·0	128·5	206·0	251·7	116·2	87·6	119·4

(continued)

Table 1: Continued

Sample	TNG113d1	TNG113d2	TNG113a1	TNG113a2	TNG113b3*	TNG113b4*	TNG113e	TNG113f*	TNG113h*	TNG113i
Rock type	Amph.	Amph.	Diatexite	Diatexite	Diatexite	Diatexite	Diatexite	Hbl-rich d.	Hbl-rich d.	Diatexite
Major Elements wt%										
SiO_2	46·90	46·50	66·80	68·40	72·20	67·40	70·60	64·70	59·00	70·40
TiO_2	1·59	1·58	0·36	0·33	0·22	0·21	0·23	0·57	0·93	0·18
Al_2O_3	17·40	17·50	18·30	17·50	16·40	18·80	16·80	15·90	15·80	17·10
Fe_2O_3t	11·80	11·50	2·18	1·77	0·97	1·40	1·39	3·65	6·53	1·09
MnO	0·18	0·18	0·03	0·02	0·02	0·02	0·02	0·06	0·12	bd
MgO	6·52	6·22	1·05	0·91	0·39	0·63	0·56	2·21	3·38	0·48
CaO	10·00	10·00	4·08	3·44	3·77	3·60	2·80	4·61	6·13	3·20
Na_2O	3·48	3·56	5·81	5·51	5·52	5·79	5·42	4·08	3·65	5·58
K_2O	1·62	1·56	1·36	1·52	0·60	2·07	1·81	3·09	3·35	1·44
P_2O_5	0·40	0·38	0·12	0·10	0·05	0·08	0·09	0·21	0·31	0·05
LOI	0·75	0·85	0·56	0·53	0·39	0·42	0·70	0·75	0·58	0·48
Total	100·60	99·83	100·65	100·02	100·52	100·45	100·45	99·86	99·78	99·97
A/CNK	0·68	0·68	0·99	1·03	0·99	1·03	1·05	0·86	0·76	1·03
Mg/(Fe + Mg)	0·52	0·52	0·49	0·50	0·44	0·47	0·44	0·55	0·51	0·47
Trace Elements ppm										
Sc	32	31	4	bd	4	0	bd	16	44	bd
Ti	8900	8832	2183	2238	2040	389	1541	5329	8953	1238
V	292	292	42	34	30	14	27	144	237	19
Cr	70	58	31	36	4	35	24	141	228	33
Mn	1499	1446	247	165	196	201	112	801	1529	90
Co	52	51	5	bd	3	6	4	16	22	1
Ni	35	31	8	7	11	27	4	87	120	5
Cu	104	46	45	20	291	136	38	5	25	5
Zn	101	98	43	41	18	28	44	69	109	30
Ga	20	19	19	18	11	18	20	20	26	18
Rb	40	35	38	48	1	7	38	43	41	35
Sr	650	724	1034	990	1392	885	1347	1019	959	967
Y	23	25	8	4	4·6	1·8	4·0	13·4	34·7	3
Zr	108	104	127	98	104	84	99	45	79	93
Nb	16	15	1	bd	5·3	0·6	bd	7·7	18·8	bd
Ba	203	227	273	332	92	458	584	744	1291	453
La	17·6**	15·2**	9·8**	10·5**	1·00	1·89	14·4**	4·66	9·03	8·6**
Ce	39**	32**	19**	21**	3·14	3·83	26**	14·11	26·66	13**
Pr	bd	bd	bd	bd	0·59	0·52	bd	2·39	4·46	bd
Nd	14**	15**	6	10**	2·80	2·20	8**	11·62	21·86	bd
Sm	4·9**	4·4**	1·6**	1·3**	1·00	0·64	1·6**	3·53	7·20	0·9**
Eu	1·6	1·4**	0·6**	0·5**	0·46	0·23	0·5**	1·16	2·21	0·4**
Gd	88	bd	bd	bd	0·86	0·51	bd	2·95	6·48	bd
Tb	bd	bd	bd	bd	0·17	0·08	bd	0·48	1·12	bd
Dy	bd	bd	bd	bd	0·98	0·44	bd	2·55	6·31	bd
Ho	bd	bd	bd	bd	0·22	0·09	bd	0·51	1·30	bd
Er	bd	bd	bd	bd	0·56	0·20	bd	1·18	3·05	bd
Tm	bd	bd	bd	bd	0·07	0·03	bd	0·14	0·37	bd
Yb	2**	1·7**	0·5**	0·2**	0·49	0·15	bd	0·90	2·27	bd
Lu	0·3**	0·32**	bd	0·09**	0·07	0·02	0·05**	0·13	0·31	bd
Pb	23	23	13	12	12·15	17·06	10	18·63	18·30	10
Th	1·7**	1·4**	3**	3·1**	0·38	0·77	3·5**	1·63	2·52	5·3**
U	bd	1·8**	1·7**	bd	0·46	0·28	2·6**	1·46	2·33	2·3**
La_n/Yb_n	5·9	6·0	13·2	35·4	1·4	8·4	n.a.	3·5	2·7	n.a
Dy_n/Yb_n	n.a	n.a	n.a	n.a	1·3	1·9	n.a.	1·8	1·8	n.a
Sum REE	n.a	n.a	n.a	n.a	12·4	10·8	n.a.	46·3	92·6	n.a

(continued)

Table 1: Continued

Sample	TNG169a*	TNG114b2*	TNG114b1*	TNG62b*	TNG113g*	TNG169b*	TNG170*	TNG171*	TNG172*	AGH23d*
Rock type	Mel. d.	Diatexite	Leucos.	Leucos.	Leucos.	Leucos.	Leucos.	Leucos.	Leucos.	Leucos.
Major Elements wt%										
SiO_2	61·95	71·00	73·10	71·80	69·50	68·02	72·09	75·53	76·93	68·74
TiO_2	0·70	0·38	0·25	0·27	0·48	0·15	0·13	0·06	0·18	0·40
Al_2O_3	14·29	15·30	14·80	16·40	16·60	17·43	15·96	14·72	14·29	14·59
Fe_2O_3t	5·18	2·39	1·51	0·43	2·06	1·91	0·71	0·39	1·13	3·34
MnO	0·15	0·04	0·02	bd	0·02	0·06	0·01	0·01	0·01	0·06
MgO	4·55	1·00	0·61	bd	1·03	0·59	0·26	0·26	0·36	1·35
CaO	6·46	2·90	2·13	2·09	3·38	4·72	2·37	2·37	2·84	3·15
Na_2O	3·01	3·89	3·34	3·73	4·99	4·87	4·33	3·57	3·95	1·87
K_2O	2·47	3·08	4·28	5·31	1·82	0·79	2·98	2·94	0·94	5·22
P_2O_5	0·14	0·10	0·07	0·02	0·14	0·11	0·03	0·02	0·04	0·08
LOI	0·93	0·51	0·47	0·35	0·67	0·56	0·47	0·34	0·45	0·47
Total	99·83	100·56	100·60	100·25	100·63	99·19	99·34	100·20	101·09	99·24
A/CNK	0·74	1·02	1·06	1·05	1·02	1·00	1·09	1·10	1·13	1·01
Mg/(Fe + Mg)	0·64	0·45	0·44	0·00	0·50	0·38	0·42	0·57	0·39	0·44
Trace Elements ppm										
Sc	21	5	2	bd	0	10	1	0	1	2
Ti	3833	3398	2206	170	193	631	553	186	692	1497
V	116	65	42	2	29	21	9	3	10	22
Cr	68	49	28	0	41	3	2	0	bd	58
Mn	1053	389	206	22	252	406	41	39	66	194
Co	51	8	5	0	8	50	69	79	81	34
Ni	112	36	18	1	40	4	3	1	2	1
Cu	22	32	60	1	193	9	40	8	16	2
Zn	46	41	24	0	38	23	8	6	14	40
Ga	17	18	23	7	13	6	20	22	7	16
Rb	46	62	48	15	9	9	52	57	27	59
Sr	558	639	607	148	619	915	1090	816	844	572
Y	22·0	10·2	4·3	0·6	3·2	14·6	1·0	1·4	0·9	3·1
Zr	24	123	88	69	225					
Nb	18·8	8·4	5·7	0·6	0·2	5·4	1·3	0·5	0·9	3·5
Ba	717	741	1260	1906	274	131	1360	1320	239	736
La	8·07	24·40	13·90	2·04	15·40	30·85	3·80	7·01	19·59	28·99
Ce	20·49	38·95	22·45	3·39	24·15	53·96	8·09	13·71	35·33	50·99
Pr	3·46	4·11	2·39	0·40	2·59	4·95	0·78	1·27	3·34	5·27
Nd	14·80	14·22	8·02	1·42	9·22	17·67	2·97	4·44	11·47	17·46
Sm	3·46	2·71	1·43	0·29	1·82	3·05	0·53	0·73	1·54	2·53
Eu	1·18	0·72	0·45	0·10	0·55	0·86	0·34	0·55	0·44	0·66
Gd	2·97	2·13	1·09	0·19	1·29	2·74	0·40	0·55	0·98	1·59
Tb	0·50	0·32	0·16	0·03	0·17	0·44	0·05	0·07	0·09	0·17
Dy	3·32	1·79	0·87	0·13	0·76	2·58	0·25	0·32	0·31	0·72
Ho	0·73	0·37	0·18	0·03	0·13	0·49	0·04	0·05	0·03	0·11
Er	2·00	0·94	0·45	0·06	0·30	1·37	0·10	0·12	0·09	0·26
Tm	0·33	0·12	0·06	0·01	0·03	0·20	0·01	0·01	0·01	0·03
Yb	2·29	0·78	0·39	0·05	0·21	1·26	0·08	0·08	0·04	0·19
Lu	0·35	0·11	0·06	0·01	0·03	0·18	0·01	0·01	0·01	0·03
Pb	13·10	16·59	19·80	4·72	13·18	10·17	15·67	14·23	9·65	26·26
Th	1·03	9·16	7·15	2·62	4·52	11·08	0·80	2·23	6·59	16·67
U	2·54	1·27	1·24	0·34	0·53	1·27	0·10	0·18	0·25	0·73
La_n/Yb_n	2·4	21·1	23·8	25·8	48·5	16·5	33·5	61·2	312·1	102·4
Dy_n/Yb_n	0·9	1·5	1·4	1·6	2·3	1·3	2·1	2·7	4·7	2·5
Sum REE	64·0	91·7	51·9	8·1	56·6	120·6	17·5	28·9	73·3	109·0

(continued)

Table 1: Continued

Sample	AGH24*	TNG60d*	AGH23a*
Rock type	Hbl-leucos.	Hbl-Kfs leucosome	
Major Elements wt%			
SiO_2	74·42	62·34	58·08
TiO_2	0·13	0·57	0·70
Al_2O_3	13·37	16·29	12·45
Fe_2O_3t	0·89	2·30	4·61
MnO	0·02	0·06	0·13
MgO	0·26	1·31	3·88
CaO	0·95	2·65	8·05
Na_2O	3·10	1·68	1·92
K_2O	4·92	10·11	6·53
P_2O_5	0·02	0·40	2·06
LOI	1·10	0·46	0·59
Total	99·16	98·14	99·01
A/CNK	1·10	0·88	0·50
Mg/(Fe + Mg)	36·66	0·53	0·63
Trace Elements ppm			
Sc	10	6	16
Ti	2307	2551	4069
V	52	38	75
Cr	44	37	61
Mn	412	349	928
Co	39	20	35
Ni	3	28	39
Cu	5	32	66
Zn	38	39	86
Ga	13	165	14
Rb	153	441	151
Sr	229	1083	903
Y	23·1	20·9	29·9
Zr			
Nb	9·0	9·7	21·2
Ba	1102	8280	4136
La	52·18	98·30	68·37
Ce	96·10	353·85	160·68
Pr	9·65	31·67	20·59
Nd	31·66	140·37	81·59
Sm	5·27	26·54	14·35
Eu	1·06	5·04	2·91
Gd	4·50	15·06	9·53
Tb	0·66	1·60	1·09
Dy	3·77	6·00	5·24
Ho	0·76	0·72	0·93
Er	2·20	1·60	2·46
Tm	0·32	0·16	0·34
Yb	1·99	0·89	2·10
Lu	0·29	0·11	0·30
Pb	28·15	85·37	30·21
Th	22·44	93·30	21·32
U	1·27	6·53	3·73
La_n/Yb_n	17·7	74·1	21·9
Dy_n/Yb_n	1·8	13·6	3·7
Sum REE	210·4	681·9	370·5

*Trace elements analyzed by ICP-MS using a Thermo Finnigan X series II, quadrupole ICP-MS system at Monash University.
**Trace elements determined by INAA of pressed whole-rock powder pellets, performed at Activation Laboratories Ltd., Ontario, Canada.
Mel., Melanosome; Amph., Amphibolite; Hbl-rich d., Hbl-rich diatexite. Leucos., Leucosome; Mel. d., Melanocratic part in diatexite; Hbl-leucos., Hbl-leucogranite; Hbl-Bt-g., Hbl-Bt granodiorite; Bt-g., Bt granodiorite.

WHOLE-ROCK GEOCHEMISTRY

Major elements

The magmatic protoliths all have similar mineral assemblages, but with varying proportions, except for clinopyroxene, which is present only in the most mafic varieties of diorites. Protolith compositional trends are generally characteristic of rocks from magmatic arcs (e.g. Debon *et al.*, 1987; Frost *et al.*, 2001). The protoliths define a broad calc-alkalic trend with some samples plotting in the calcic and some in the alkali–calcic field in an alkali–lime diagram (Frost *et al.*, 2001; see fig. 9b of Reichardt *et al.*, 2010); here we use the term calc-alkalic for simplicity.

The protoliths, leucosomes and melanosomes plot in distinct fields in a number of geochemical variation diagrams, whereas the diatexites are intermediate between leuco- and melanosome. In an $Fe_2O_3 + MgO + TiO_2$ vs SiO_2 diagram (Fig. 5a), the melanosomes have the highest Fe–Mg–Ti contents, the protoliths define a field of intermediate values, and the leucosomes have the lowest values. The lowest SiO_2 contents (46·2 and 46·9 wt %) are recorded by two amphibolite schollen in diatexite, whereas the highest values are found in leucosomes. The leucogranitic rocks are generally mildly peraluminous, whereas the protoliths are metaluminous (Reichardt *et al.*, 2010). A $CaO + Na_2O$ vs K_2O diagram (Fig. 5b) shows trends compatible with K-feldspar accumulation in the Hbl–Kfs leucosomes, and plagioclase accumulation in tonalitic, Hbl-free leucosomes and Hbl-bearing diatexites. Relative to the protoliths, the granitic leucosomes are depleted in $CaO + Na_2O$ but strongly enriched in K_2O. Conversely, the tonalitic leucosomes are depleted in K_2O and enriched in $CaO + Na_2O$. Amphibolites and quartz-diorites have the highest $CaO + Na_2O$ values, which is consistent with their higher abundances of hornblende, titanite and occasional clinopyroxene.

Trace elements

Protoliths and neosomes also vary systematically in terms of their trace element concentrations. Figure 6 compares the La_n/Yb_n and Sr/Y values of Karakoram Shear Zone leucogranites with their inferred protoliths. Most of the leucocratic anatectic rocks (neosomes) plot in the field of Archean TTGs and adakites, whereas the protoliths plot in the field of arc-related rocks. Quartz-diorite and granodiorite protoliths show roughly subparallel and moderately fractionated REE patterns (Fig. 6a; $La_n/Yb_n = 17·5–32·7$) with slightly concave-upward middle REE (MREE) to HREE patterns and weak negative Eu anomalies (Eu/Eu* = 0·7–0·8) (Fig. 7a). Amphibolite schollen are the least fractionated rocks (Fig. 7b; $La_n/Yb_n = 5·1–7·7$).

Melanocratic, Hbl-rich parts of diatexites (samples TNG113f, TNG113h, TNG169a) show slight light REE (LREE) depletion relative to MREE with concave-downward REE patterns, leading to low La_n/Yb_n values

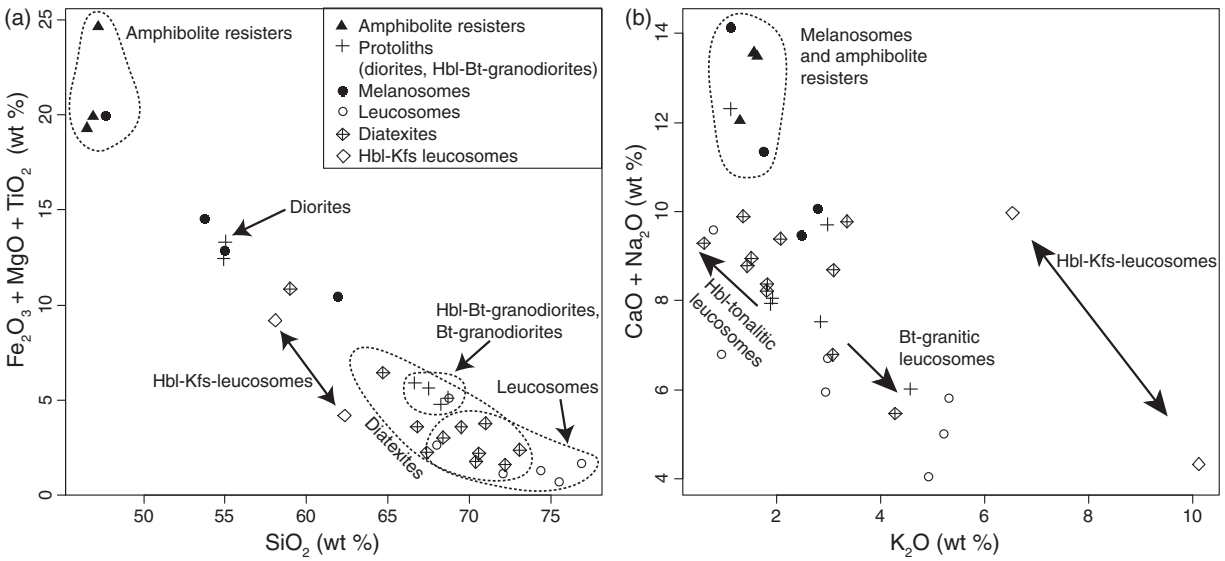

Fig. 5. (a) $Fe_2O_3 + MgO + TiO_2$ vs SiO_2 diagram indicating decrease of ferromagnesian and titaniferous phases with increasing silica content. (b) $CaO + Na_2O$ vs K_2O wt % diagram showing a central field of Hbl–Bt-granodiorite protoliths and melanosomes overlapping with diatexites. The arrow towards higher K_2O indicates accumulation of K-feldspar in leucosomes. Plagioclase accumulation in diatexites is indicated by the arrow in the opposite direction. High hornblende contents contribute to high $CaO + Na_2O$ contents in diorites and amphibolite resisters. The two samples of Hbl–Kfs leucosome show extremely high K_2O, and variable $CaO + Na_2O$ concentrations reflecting variations in Kfs and Hbl contents. Symbols as in (a).

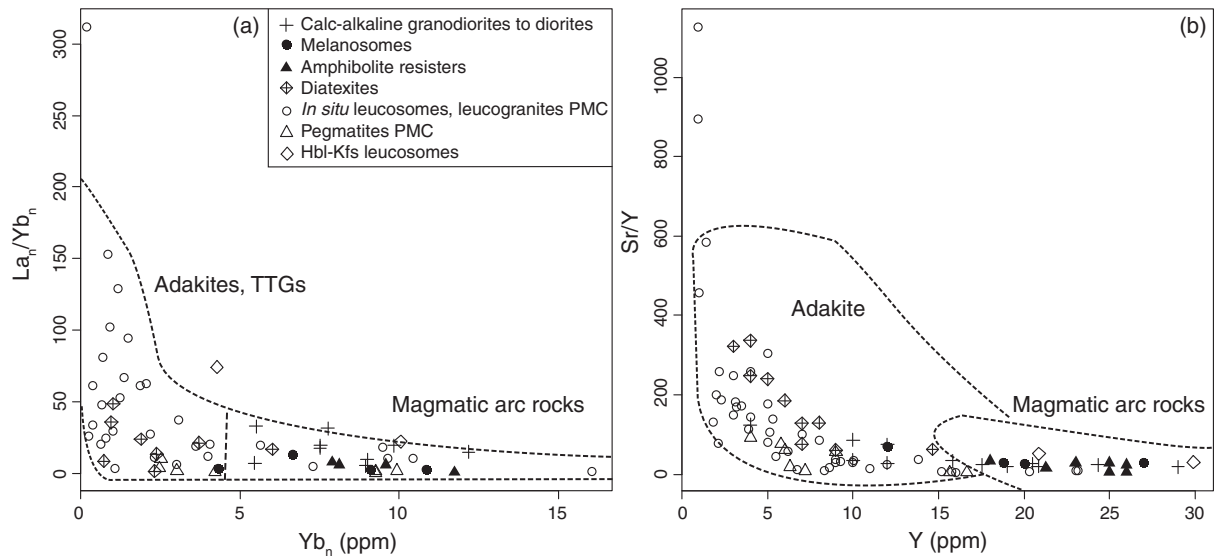

Fig. 6. (a) La_n/Yb_n vs Yb_n variation in calc-alkaline arc rocks and leucogranites of the PMC. Leucogranites from the Karakoram Batholith are also included. Normalization after the chondrite values of Boynton (1984) (For geochemical data for leucogranites of the PMC and Karakoram Batholith see Table 1 in Reichardt *et al.* (2010)). Symbols as in Fig. 5 except for open triangles, which indicate pegmatite dykes. Fields for magmatic arc rocks and for adakites and TTGs are taken from Defant *et al.* (2002). (b) Sr/Y vs Y diagram.

(Fig. 7c; $La_n/Yb_n = 2{\cdot}4$–$3{\cdot}5$). Interestingly, this pattern is comparable with the REE patterns for hornblende (see below), suggesting the importance of hornblende for the REE budget of these rocks (Hilyard *et al.*, 2000).

Hornblende-free, tonalitic leucosomes have steep, strongly fractionated REE patterns with La_n/Yb_n varying from 33 to 312 (Fig. 7d); in contrast, hornblende-bearing leucosomes have La_n/Yb_n values ranging from 1·4 to 74·1 (Table 1). Hbl-free, tonalitic leucosomes also have pronounced positive Eu anomalies (Fig. 7d), indicative of plagioclase accumulation, in agreement with the observed Sr enrichment (samples TNG170, TNG171; Table 1).

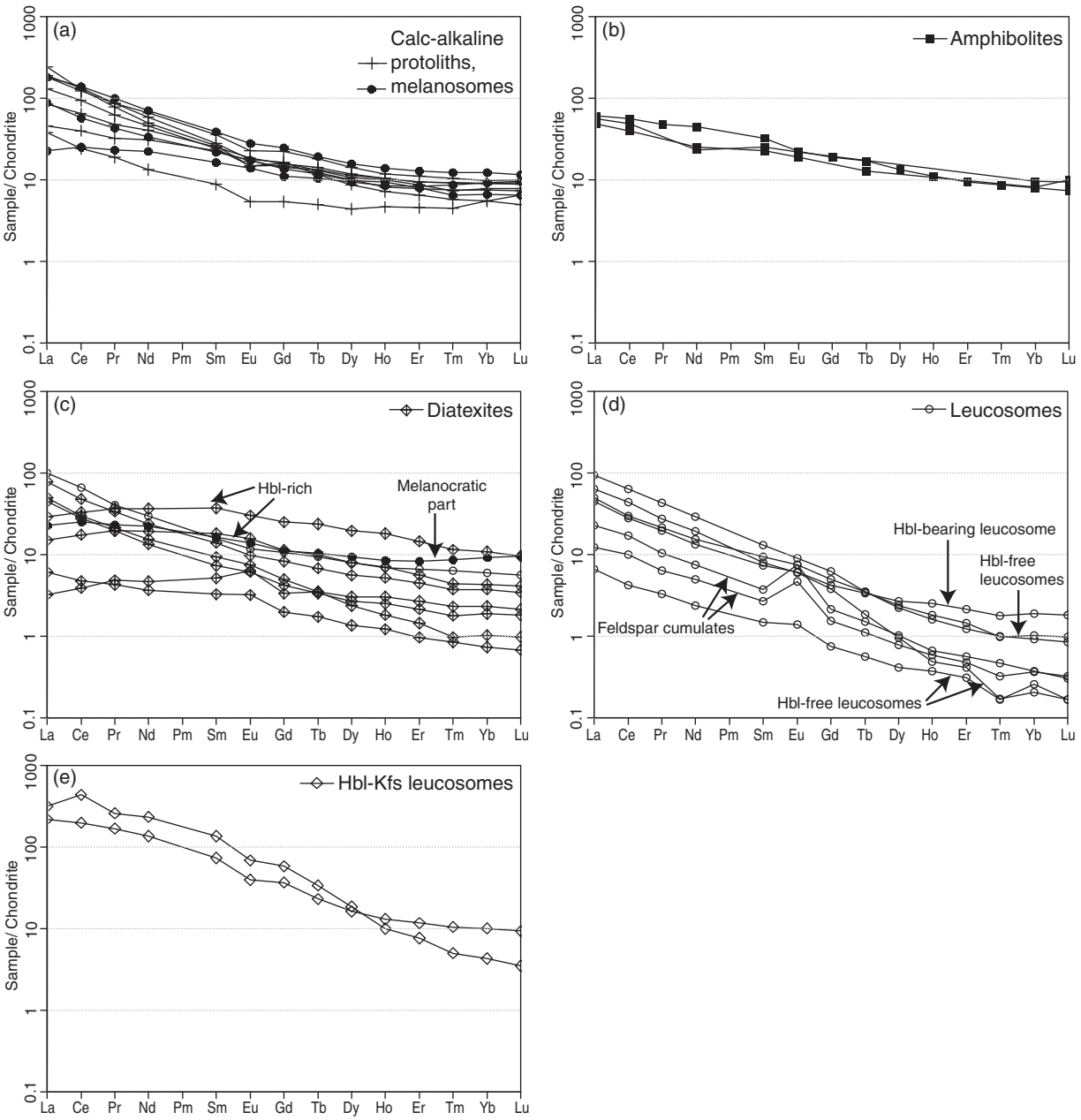

Fig. 7. Chondrite-normalized REE patterns: (a) protoliths and melanosomes; (b) amphibolite resisters; (c) diatexites; (d) leucosomes. (Note lower HREE values for Hbl-free leucosomes compared with Hbl-bearing leucosomes.) (e) Hbl–Kfs leucosomes contain unusually high amounts of Ap, Aln and Ttn. Data are given in Table 1. Chondrite normalization after Boynton (1984).

Because of their Y depletion compared with the protoliths, these rocks yield the highest Sr/Y ratios in the region (Sr/Y = 583·5–1127·5 in Fig. 6). The Hbl–Kfs leucosomes (Fig. 7e) are rich in accessory phases such as apatite and titanite and show anomalous trace element contents, particularly enrichment in LREE (Fig. 7e). These rocks are also strongly enriched in Ba, Rb, Sr and P_2O_5, relative to the inferred protoliths (see Table 1).

Melanosomes and amphibolite schollen have the lowest contents of LILE (Fig. 8a). Diatexites and leucosomes are generally enriched in Ba and Sr, but depleted in Rb compared with the protoliths, in agreement with water-fluxed melting, which leads to high Sr/Rb values because of the prevalence of feldspars over micas in the melting reaction (Patiño Douce & Harris, 1998). Strong Ba and Rb enrichment, however, are observed in the Hbl–Kfs leucosomes

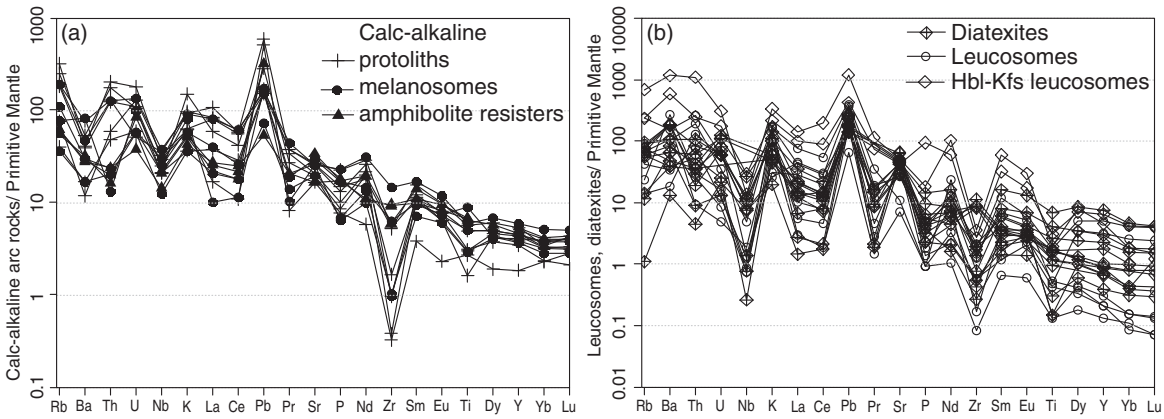

Fig. 8. Multielement diagrams normalized to primitive mantle after Sun & McDonough (1989). (a) Amphibolite resisters, protoliths and melanosomes. (b) Diatexites and leucosomes. Note extreme LILE enrichments in the Hbl–Kfs leucosomes. Lowest Nb, Ti and Zr values are recorded for leucosomes that show feldspar accumulation.

(Fig. 8b). High Ba and Sr values correlate with high values for K_2O, $CaO + Na_2O$ and Al_2O_3, and modelling for leucogranites in the PMC has shown that these values are indicative of K-feldspar and plagioclase accumulation, respectively (Reichardt *et al.*, 2010).

Fractionation trends are also apparent for compatible elements, with the highest concentrations of V, Cr and Ni in the amphibolite resisters (Fig. 8a). The HFSE Ti and Zr are generally enriched in the melanosomes compared with the protoliths, suggesting accumulation of accessory phases in the melanosomes. Concentrations of Nb are variable, showing no trend in protoliths and melanosomes. Leucosomes have the lowest concentrations of HFSE. Diatexites show variable HFSE contents (Fig. 8b) that can be attributed to different amounts of mafic residual minerals from the protolith found in schlieren and disaggregated in the groundmass, consisting mostly of hornblende, biotite, titanite and accessory minerals. This explains the range of HFSE contents, including the overlap with protolith values. In the following section we investigate the mineral chemistry and the contribution of the various minerals to the whole-rock trace element contents.

MINERAL COMPOSITION

Major elements

Hornblende

All analysed amphiboles are calcic ($CaO = 10{\cdot}91–12{\cdot}10$ wt %, Table 2), and according to the classification scheme of Leake *et al.* (1997) most are ferropargasites [$Ca > 1$, $Na + K > 0{\cdot}5$, $X_{Mg} < 0{\cdot}5$, where $X_{Mg} = Mg/(Mg + Fe_{tot})$, and Si between 5·5 and 6·5 atoms per formula unit (a.p.f.u.)] or straddle the boundary to the field of pargasite ($X_{Mg} > 0{\cdot}51$) (Fig. 9). The amphiboles show a trend from ferropargasites through pargasite to edenite with increasing Si and X_{Mg}, except for amphiboles from a Hbl-leucogranite from the Rongdu location within the Karakoram Batholith (sample AGH24) that have lower X_{Mg} and lie in the field of ferro-edenite. Generally, ferro-edenite grains from the Rongdu location (Fig. 1; samples AGH23a, AGH24) show a wide range of Si contents. Amphibole grains in one Hbl–Kfs leucosome from the Tangtse area (sample TNG165) also have widely varying Si contents. High Si is generally coupled with low total Al content. Alkali ($Na + K$) contents range between 0·91 and 0·30 a.p.f.u. and correlate positively with aluminium contents, but negatively with silica contents (Fig. 10a), reflecting a trend common for calcic amphiboles in calc-alkaline magmas (Femenias *et al.*, 2006). A similar trend is observed for Ti contents (Fig. 10b). For simplicity we subsequently refer to all amphibole varieties as hornblende.

Total aluminium contents (Al_{tot}) vary between 1·07 and 2·28 a.p.f.u. in samples from the Tangtse gorge area (TNG59, TNG60c, TNG60d, TNG165, TNG169a, TNG169b, TNG203, TNG204c), and between 0·87 and 1·5 a.p.f.u. for the Rongdu location (AGH23a, AGH24). In a sample of ~2 cm wide leucosome in a mafic diorite (sample TNG165), the hornblende grains show a trend towards higher Al contents and lower X_{Mg} from the centre towards the melanosome rims. A significant difference between the hornblende composition in melanosome and leucosome is apparent in a diatexite that has diorite as its most probable protolith (samples TNG169a and TNG169b, respectively). Here, grains in the leucosome have higher Fe and lower Mg contents.

The Al_{tot} values were used to estimate the crystallization pressure using the Al-in-hornblende geobarometer (Hammarstrom & Zen, 1986; Schmidt, 1992). The required mineral paragenesis for use of this equation, $Hbl + Bt + Pl + Qtz + Ttn + Mgt$ (or Ilm), is present in all the studied thin sections. For these estimates, the rim of a growing crystal that is in equilibrium contact

Table 2: Major element concentrations of hornblende

Sample:	TNG59	TNG169a	TNG169b	TNG203	TNG165	TNG204c	TNG60c	TNG60d	AGH23a	AGH24
Average of *n* analyses:	$n=7$	$n=5$	$n=7$	$n=8$	$n=12$	$n=10$	$n=4$	$n=18$	$n=6$	$n=8$
Oxides										
SiO_2	41·62 ± 0·69	43·87 ± 1·31	40·06 ± 0·32	42·73 ± 0·65	44·80 ± 2·39	40·71 ± 0·55	40·11 ± 0·39	42·33 ± 1·23	46·89 ± 1·52	45·36 ± 1·43
TiO_2	0·93 ± 0·08	1·03 ± 0·14	1·43 ± 0·02	0·78 ± 0·03	0·68 ± 0·16	1·10 ± 0·12	0·81 ± 0·03	0·61 ± 0·06	0·71 ± 0·15	1·43 ± 0·54
Al_2O_3	10·97 ± 0·54	10·60 ± 1·04	12·48 ± 0·29	10·27 ± 0·61	9·42 ± 1·97	11·79 ± 0·51	11·54 ± 0·10	10·24 ± 0·29	6·92 ± 1·05	7·40 ± 1·08
V_2O_3	0·05 ± 0·01	0·05 ± 0·02	0·04 ± 0·03	0·06 ± 0·02	0·03 ± 0·02	0·08 ± 0·03	0·05 ± 0·01	0·05 ± 0·02	0·02 ± 0·02	0·05 ± 0·02
Cr_2O_3	0·02 ± 0·03	0·04 ± 0·02	0·00 ± 0·01	0·09 ± 0·05	0·12 ± 0·06	0·03 ± 0·02	0·01 ± 0·02	0·05 ± 0·03	0·03 ± 0·01	0·01 ± 0·01
FeO	19·56 ± 0·19	15·34 ± 1·02	20·14 ± 0·11	17·15 ± 0·83	15·07 ± 1·10	19·09 ± 0·28	21·01 ± 0·18	15·67 ± 1·31	15·38 ± 0·77	19·26 ± 0·51
MnO	0·51 ± 0·05	0·53 ± 0·05	0·74 ± 0·06	0·33 ± 0·08	0·38 ± 0·03	0·35 ± 0·03	0·34 ± 0·02	0·41 ± 0·05	0·40 ± 0·03	0·49 ± 0·08
MgO	9·51 ± 0·29	11·83 ± 0·91	8·01 ± 0·13	11·02 ± 0·62	12·55 ± 1·28	8·90 ± 0·33	8·31 ± 0·09	11·45 ± 0·17	13·38 ± 0·78	10·68 ± 0·68
CaO	11·68 ± 0·08	11·81 ± 0·16	11·33 ± 0·11	11·59 ± 0·10	11·83 ± 0·15	11·61 ± 0·16	11·33 ± 0·05	11·47 ± 0·59	11·83 ± 0·12	11·30 ± 0·30
Na_2O	1·50 ± 0·08	1·39 ± 0·12	1·45 ± 0·04	1·77 ± 0·06	1·69 ± 0·20	1·31 ± 0·07	1·82 ± 0·02	1·76 ± 0·05	1·66 ± 0·14	1·23 ± 0·28
K_2O	1·54 ± 0·19	1·28 ± 0·18	1·79 ± 0·10	1·50 ± 0·13	1·27 ± 0·33	1·63 ± 0·13	1·80 ± 0·05	1·50 ± 0·09	0·93 ± 0·17	0·87 ± 0·20
NiO	0·01 ± 0·01	0·03 ± 0·02	0·01 ± 0·01	0·05 ± 0·02	0·08 ± 0·01	0·02 ± 0·01	0·02 ± 0·02	0·05 ± 0·03	0·02 ± 0·02	0·01 ± 0·01
ZnO	0·04 ± 0·04	0·05 ± 0·04	0·03 ± 0·03	0·02 ± 0·02	0·05 ± 0·05	0·04 ± 0·04	0·05 ± 0·04	0·05 ± 0·03	0·05 ± 0·06	0·03 ± 0·03
Nb_2O_5	0·00 ± 0·01	0·01 ± 0·01	0·02 ± 0·02	0·03 ± 0·04	0·02 ± 0·02	0·01 ± 0·02	0·03 ± 0·02	0·01 ± 0·02	0·05 ± 0·06	0·01 ± 0·01
Cations										
Si	6·27 ± 0·08	6·47 ± 0·14	6·11 ± 0·04	6·42 ± 0·07	6·60 ± 0·28	6·23 ± 0·06	6·17 ± 0·03	6·44 ± 0·05	6·87 ± 0·17	6·73 ± 0·16
Ti	0·11 ± 0·01	0·11 ± 0·02	0·16 ± 0·00	0·09 ± 0·00	0·07 ± 0·02	0·13 ± 0·01	0·09 ± 0·00	0·07 ± 0·01	0·08 ± 0·02	0·16 ± 0·06
Al_{tot}	1·95 ± 0·10	1·84 ± 0·20	2·24 ± 0·05	1·82 ± 0·11	1·64 ± 0·36	2·13 ± 0·10	2·09 ± 0·02	1·84 ± 0·04	1·20 ± 0·19	1·30 ± 0·20
Cr	0·00 ± 0·00	0·01 ± 0·00	0·00 ± 0·00	0·01 ± 0·01	0·01 ± 0·01	0·00 ± 0·00	0·00 ± 0·00	0·01 ± 0·00	0·00 ± 0·00	0·00 ± 0·00
Fe_{tot}	3·25 ± 0·07	2·50 ± 0·17	3·30 ± 0·05	2·79 ± 0·11	2·39 ± 0·20	3·09 ± 0·07	3·46 ± 0·03	2·58 ± 0·14	2·43 ± 0·15	3·20 ± 0·16
Mn	0·07 ± 0·01	0·07 ± 0·01	0·10 ± 0·01	0·04 ± 0·01	0·05 ± 0·00	0·05 ± 0·00	0·04 ± 0·00	0·05 ± 0·01	0·05 ± 0·00	0·06 ± 0·01
Mg	2·14 ± 0·05	2·60 ± 0·18	1·82 ± 0·03	2·47 ± 0·14	2·75 ± 0·25	2·03 ± 0·07	1·90 ± 0·02	2·60 ± 0·07	2·92 ± 0·15	2·36 ± 0·13
Ca	1·89 ± 0·02	1·87 ± 0·02	1·85 ± 0·02	1·86 ± 0·01	1·87 ± 0·01	1·90 ± 0·02	1·87 ± 0·01	1·87 ± 0·04	1·86 ± 0·01	1·80 ± 0·05
Na	0·44 ± 0·03	0·40 ± 0·04	0·43 ± 0·01	0·51 ± 0·02	0·48 ± 0·06	0·39 ± 0·02	0·54 ± 0·01	0·52 ± 0·02	0·47 ± 0·04	0·35 ± 0·08
K	0·30 ± 0·04	0·24 ± 0·04	0·35 ± 0·02	0·29 ± 0·02	0·24 ± 0·06	0·32 ± 0·03	0·35 ± 0·01	0·29 ± 0·01	0·17 ± 0·03	0·17 ± 0·04
Ni	0·00 ± 0·00	0·00 ± 0·00	0·00 ± 0·00	0·01 ± 0·00	0·01 ± 0·00	0·00 ± 0·00	0·00 ± 0·00	0·01 ± 0·00	0·00 ± 0·00	0·00 ± 0·00
X_{Mg}	0·40 ± 0·01	0·51 ± 0·03	0·36 ± 0·00	0·47 ± 0·02	0·53 ± 0·04	0·40 ± 0·01	0·35 ± 0·00	0·50 ± 0·02	0·55 ± 0·03	0·42 ± 0·02

Cations recalculated on the basis of 23 oxygen atoms; ± is one standard deviation. Complete analysis is given in Supplementary Data Appendix 2.

with the last phase to crystallize, usually quartz, is most likely to record the pressure of solidification of the rock (Johnson & Rutherford, 1989). Pressure determinations were carried out using the equation of Schmidt (1992):

$$P(\text{kbar}) = 4{\cdot}76\text{Al}_{\text{tot}} - 3{\cdot}01.$$

These calculations yield pressures for rocks in the Tangtse area that are consistently higher than those obtained for samples from the Rongdu area. In samples from the anatectic region exposed in the Tangtse area, line analyses and single rim analyses of hornblende grains (sample TNG60d, Supplementary Data Appendix 2) show uniform major element concentrations throughout the grains, and no significant variation in Al_{tot} when comparing rims in contact with different minerals (Fig. 11a). This homogeneity is indicative of equilibrium during crystal growth (Spear, 1981). Hence, we use the average value from the line scans of this sample (TNG60d) for pressure estimation, and these yield 5·7 ± 0·2 kbar ($n=43$). In contrast, line analyses of hornblendes from the Karakoram Batholith in the Rongdu area generally show significantly lower values for Al_{tot}, but also show relatively large variations without obvious trends from core to rim (Fig. 11b). We therefore cannot reliably quantify the pressure difference between the Tangtse and Rongdu areas. However, zonation from core to rim with systematic changes of

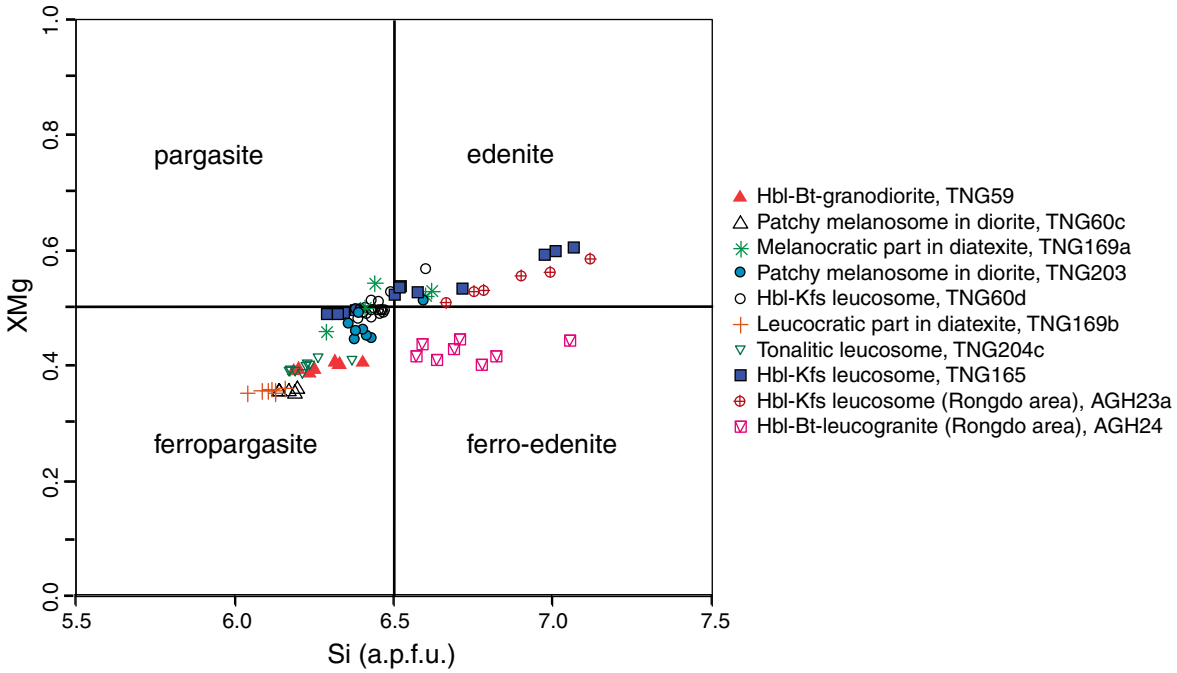

Fig. 9. Hornblende classification after Leake *et al.* (1997). Fe used to calculate X_{Mg} is Fe_{tot}. Values given in atoms per formula unit (a.p.f.u.) calculated for 23 oxygen atoms (Table 2).

major element concentrations is apparent in one line analysis from one of these samples (Fig. 11c). For this grain, calculation of the equilibration pressure based on the rim compositions ($Al_{tot} \sim 1{\cdot}3$ a.f.p.u.) yielded pressures of 3·2 and 3·3 kbar, respectively, but with a large estimated uncertainty (sample AGH24, Supplementary Data Appendix 2). These results suggest that the hornblende in the Karakoram Batholith may have crystallized at ~2 kbar lower pressure than that in the Tangtse area. This difference is in agreement with the expectation that the anatectic source regions of leucogranites, such as in the Tangtse area, are generally deeper than emplacement levels, such as the Rongdu area (Reichardt *et al.*, 2010).

Plagioclase

Plagioclase grains were analysed from 10 samples. Anorthite contents are higher in melanosomes in diorites compared with more silica-rich Bt-granodiorites (Fig. 12). Plagioclase grains in a Bt-granodiorite protolith (whole-rock $SiO_2 = 67{\cdot}5$ wt %) show compositional ranges (An = 22·7–29·1) expected for plutonic rocks of a calc-alkaline differentiation series (Bowen, 1919). Plagioclase in a melanocratic part of a diatexite has only slightly higher anorthite contents (An = 25·2–29·4) than in its leucocratic part (An = 24·3–28·9). Such small differences between melanosome and leucosome have been reported from migmatites formed by both water-present and water-absent partial melting (Gupta & Johannes, 1982; Kenah & Hollister, 1983; Johannes *et al.*, 2003), suggesting that the plagioclase in the melanosome equilibrated with a percolating melt (Marchildon & Brown, 2001). It is also possible that the plagioclase in the patchy melanosome is not residual, but a melting product. The leucosome in a diffuse, patchy migmatitic diorite contains plagioclase with An = 17·4–24·5. A Hbl–Kfs leucosome in a mafic diorite has the most sodic plagioclase, found only as small grains in interstices or as thin overgrowths on K-feldspar (An = 1·4–19·7). Thin albite rims are also present in Hbl–Kfs leucosome patches in the diorite with a mottled texture in Fig. 3b. These data indicate that, in general, plagioclase in the leucosomes is less calcic than in the protoliths and melanosomes, and that albite is found only as small grains in some unusual leucosome types.

Trace element geochemistry

Trace elements are useful indicators of partial melting processes. In order to better understand these processes, we undertook mineral analysis using LA-ICP-MS. We report trace element concentrations of the main mineral phases in the migmatites of the PMC with particular emphasis on hornblende (Table 3). Abnormal analyses where the laser hit an inclusion, leading to extreme values for certain trace elements (e.g. Zr for zircon, La, Ce and Th for allanite and Ba for K-feldspar), have been omitted from the results.

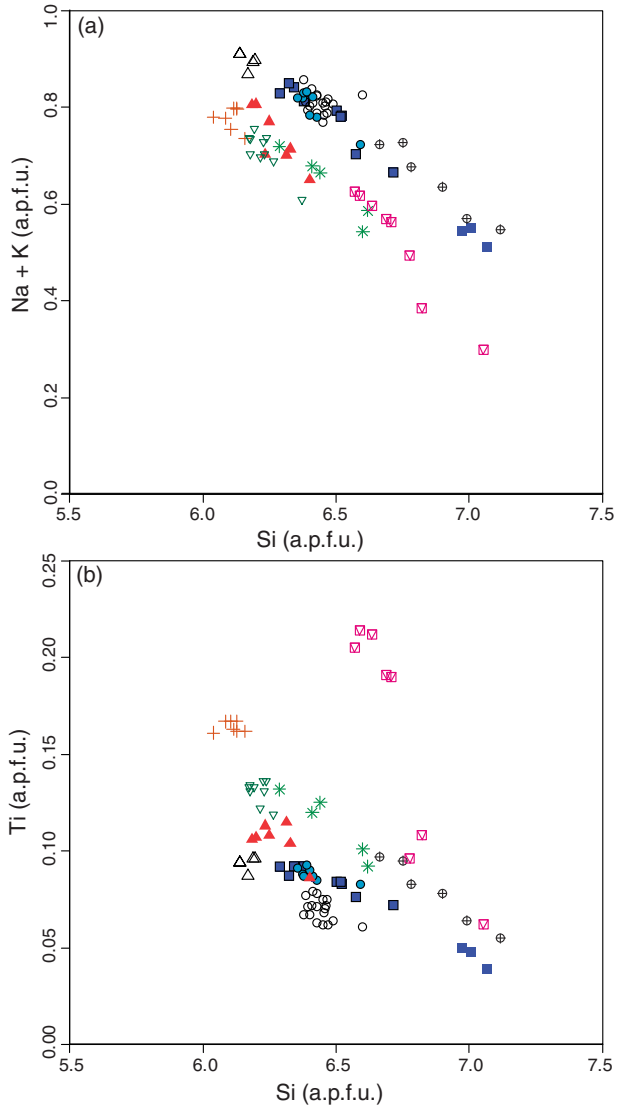

Fig. 10. Major element variations in hornblende: (a) Na + K vs Si; (b) Ti vs Si. Symbols as in Fig. 9.

Hornblende

Hornblendes were analysed from eight samples and show large variations in trace element contents, and distinct patterns in chondrite-normalized REE and multi-element profiles (Figs 13 and 14). This variety of curve shapes is rather surprising and in sharp contrast to data from the literature where hornblende has a trace element pattern that corresponds closely to that predicted from solid–liquid partition coefficients ($D^{S/L}$) characterized by a well-defined bell-shaped, concave-downward REE pattern, with a maximum around the MREE (e.g. Hilyard *et al.*, 2000; Tiepolo *et al.*, 2007).

In terms of REE patterns, it is possible to group together hornblendes from a Hbl–Bt-granodiorite, a melanocratic and leucocratic part of a diatexite and a patchy, tonalitic leucosome in a diatexite (first four samples in Table 3). These show rising concentrations from the LREE to the MREE defining a concave-downward curve, followed by a relatively flat (gently upward or downward) trend from the MREE to the HREE, without the expected peak in values around Gd to Dy (Fig. 13a–d). The averages of the analyses of these four samples have La_n/Yb_n values of $0{\cdot}4 \pm 0{\cdot}2$, $0{\cdot}6 \pm 0{\cdot}3$, $0{\cdot}1 \pm 0{\cdot}0$ and $0{\cdot}3 \pm 0{\cdot}1$ (Fig. 13a–d; Table 3). These samples have HREE enrichments reaching ~70 times chondrite values in hornblendes of the leucocratic part of a diatexite (sample TNG169b, Fig. 13c). Despite some similarities in the overall shape of the REE pattern, the Hbl–Bt-granodiorite (sample TNG59, Fig. 13a) is the only sample that contains hornblendes with positive Eu anomalies (average $Eu/Eu^* = 1{\cdot}5 \pm 0{\cdot}4$). Concentrations of LILE (Rb, Ba and Sr) of the four grouped samples (TNG59, TNG169a, TNG169b, TNG204c) are all comparable (Fig. 14). However, both the leucocratic and melanocratic parts of the diatexite (samples TNG169b, TNG169a) show much higher Nb and Ta contents, and lower Th contents than the hornblende of all other samples.

Another distinct group comprises hornblendes from Hbl–Kfs leucosomes and a patchy melanosome in a dioritic protolith bordering a Hbl–Kfs leucosome. These have wave-shaped REE patterns (Fig. 13e–g) with concave-downward LREE to MREE curves and concave-upward MREE to HREE curves. Whereas the REE patterns of the Hbl–Kfs leucosome and the bordering patchy melanosome (Fig. 13e and g) in the Tangtse area are essentially similar, the Hbl–Kfs leucosome from the Karakoram Batholith, Rongdu location (AGH23a, Fig. 13f) shows enrichment in LREE and a decrease toward the MREE.

Sample AGH24, a Hbl–Bt-leucogranite from the Rongdu location (Fig. 13h; $SiO_2 = 74{\cdot}4$ wt %) contains hornblende that is completely different from all the other analysed samples. These grains are extremely enriched in Nb and Ta, and REE (sum $REE = 1045 \pm 190$ ppm) are one order of magnitude more abundant than the highest total REE concentration reached in the other samples (94 ± 16 ppm for sample TNG169b). The overall shape is moderately concave downward with a strong negative Eu anomaly ($Eu/Eu^* = 0{\cdot}2 \pm 0{\cdot}0$). La_n/Yb_n values are on average $1{\cdot}8 \pm 0{\cdot}2$.

REE patterns of other minerals

Plagioclase from a patchy leucosome and a patchy melanosome in diorite shows low REE concentrations except for Eu (Fig. 15). Clinopyroxene exhibits wave-like REE patterns with concave-downward LREE to MREE and concave-upward MREE to HREE patterns and overall moderate REE contents (sum REE 16 and 21 ppm, Fig. 15). REE contents in biotite were generally too low to yield reliable results except for two analyses (Fig. 15). One

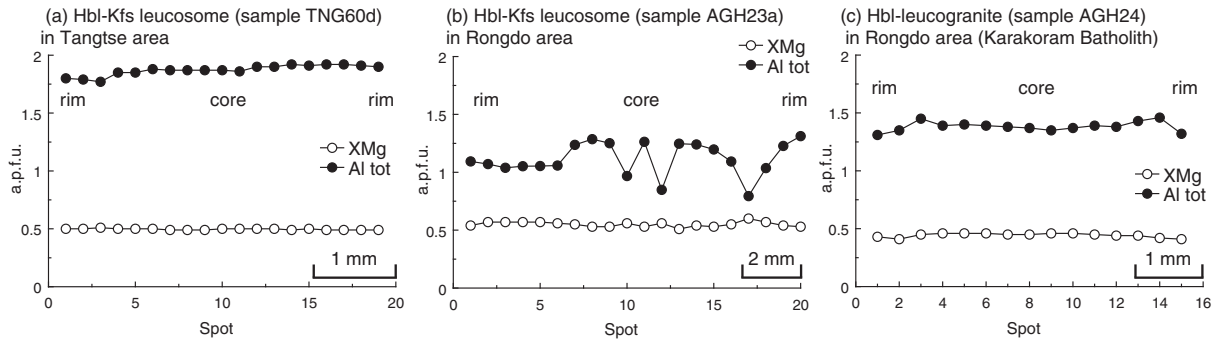

Fig. 11. Examples of microprobe traverses of hornblende grains. (a) Large, poikilitic hornblende in Hbl–Kfs leucosome in the Tangtse area. (b) Hornblende grain with slight patchy irregular zoning in Hbl–Kfs leucosome in migmatite block from inside the Karakoram Batholith, Rongdu area. (c) Brown–green hornblende with green rims in Hbl-leucogranite of the Karakoram Batholith, Rongdu area. Note lower Al_{tot} contents in hornblende from Rongdu area (b and c) compared with the Tangtse area (a). Hornblende in (a) has uniform Al_{tot} and X_{Mg} concentration throughout the grain, indicating equilibrium during growth. This is in contrast to hornblende in (b), which has high variations in Al_{tot}. Hornblende in (c) shows slightly lower Al_{tot} on rims, compared with centre of grain. (For analysis details see Supplementary Data Appendix 2.)

from a Hbl–Bt-granodiorite protolith shows a flat REE pattern (sample TNG59), whereas the other from a Hbl–Bt-leucogranite from the Karakoram Batholith, Rongdu area (sample AGH24) shows a relatively flat REE pattern, a positive Eu anomaly (Eu/Eu* = 2·2) and REE concentrations on average more than 100 times chondrite values. Overall REE enrichment is unusual for biotite (e.g. Gromet & Silver, 1983), and we note that unusual REE enrichment was also found in hornblende from the same sample (AGH24). Trace elements that indicate micro-inclusions of accessory minerals (e.g. Zr for zircon or Th for Aln) were not observed in the analysis. Despite the presence of these REE-rich hornblendes and biotites, the whole-rock REE pattern of this sample shows higher values only of HREE, but not of LREE, when compared with the leucogranites of the PMC (Table 1).

Our results for titanite and allanite (Fig. 15b) compare well with the results of Gromet & Silver (1983). Titanite shows an overall REE enrichment of more than 1000 times chondrite values and negative Eu anomalies (Eu/Eu* between 0·5 and 0·7). We obtained two analyses of allanite grains from Hbl–Kfs leucosomes (samples TNG60d, AGH23a). These show extreme enrichment in LREE, reaching around 10^5 chondrite values for La and Ce, and strong fractionation of LREE over HREE ($La_n/Yb_n = 5603·7$). High La and Ce concentrations are part of the stoichiometry of allanite. The allanite grains also show extremely high Th concentrations (see Supplementary Data Appendix 4), indicating the potential control of allanite on the whole-rock Th budget (Hermann, 2002).

The influence of titanite and allanite on whole-rock REE contents is particularly evident in the Hbl–Kfs leucosomes (TNG60d, AGH23a) that are rich in these accessory phases, and that show LREE enrichment, and the highest total REE and Th contents of all the analysed whole-rocks (Fig. 7e; Table 1). Interestingly, the only hornblende that has LREE enrichment over the MREE and HREE was found in an allanite-bearing Hbl–Kfs leucosome (sample AGH23a). In the following discussion we use geochemical model calculations to evaluate the significance of different mineral modal contents in the partial melting residue and entering the melt based on data from the literature as well as our own analyses.

GEOCHEMICAL MODELLING

Models can be used to simulate partial melting of known source rocks and the compositions of the melt products or to identify unknown sources. In the PMC, the field relations allow us to choose appropriate samples that exemplify the likely source rocks, the *in situ* melt products (leucosome) and residual rocks (melanosome). However, approaches to model the complicated processes involved in crustal partial melting have the intrinsic risk of oversimplification. Despite these limitations, relatively simple model calculations can be used to test assumptions based on field observations and to test the interpretation of the geochemical data. We therefore applied models to reproduce the geochemical characteristics of the melts originating from the migmatites in the PMC, focusing particularly on the role of hornblende.

Batch melting

For modelling partial melting we used the equilibrium batch melting equation of Shaw (1970):

$$C_L^i = \frac{C_0^i}{D_{(bulk)} + F(1 - D_{(bulk)})}$$

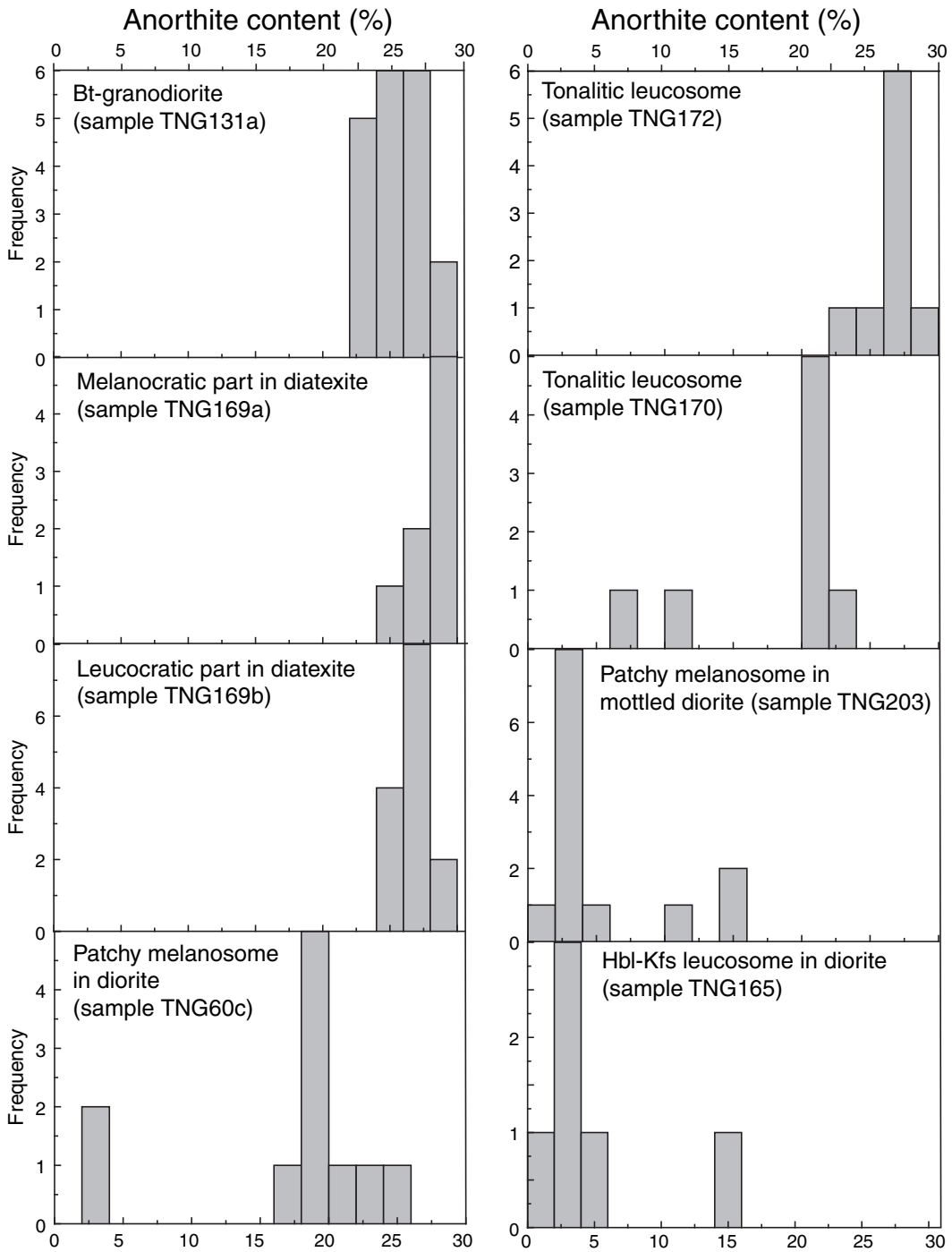

Fig. 12. Anorthite contents of plagioclase. Note overlap in Bt-granodiorite, melanosome and leucosome. Analysis details are given in Supplementary Data Appendix 3.

where C_L represents the concentration of element i in the liquid in relation to its concentration in the initial solid C_0. The amount of partial melting is given as the fraction F, and all minerals contribute to the melt according to their modal proportion in the protolith. The partition coefficient $D_{(bulk)}$ of element i is the sum of the D values for each mineral, multiplied by its weight proportion in the residual solid ($D_{(bulk)} = \sum D_{RS} X_{RS}$). This calculation is sensitive to only the modal proportions of the minerals in the model residue and the bulk partition coefficient of

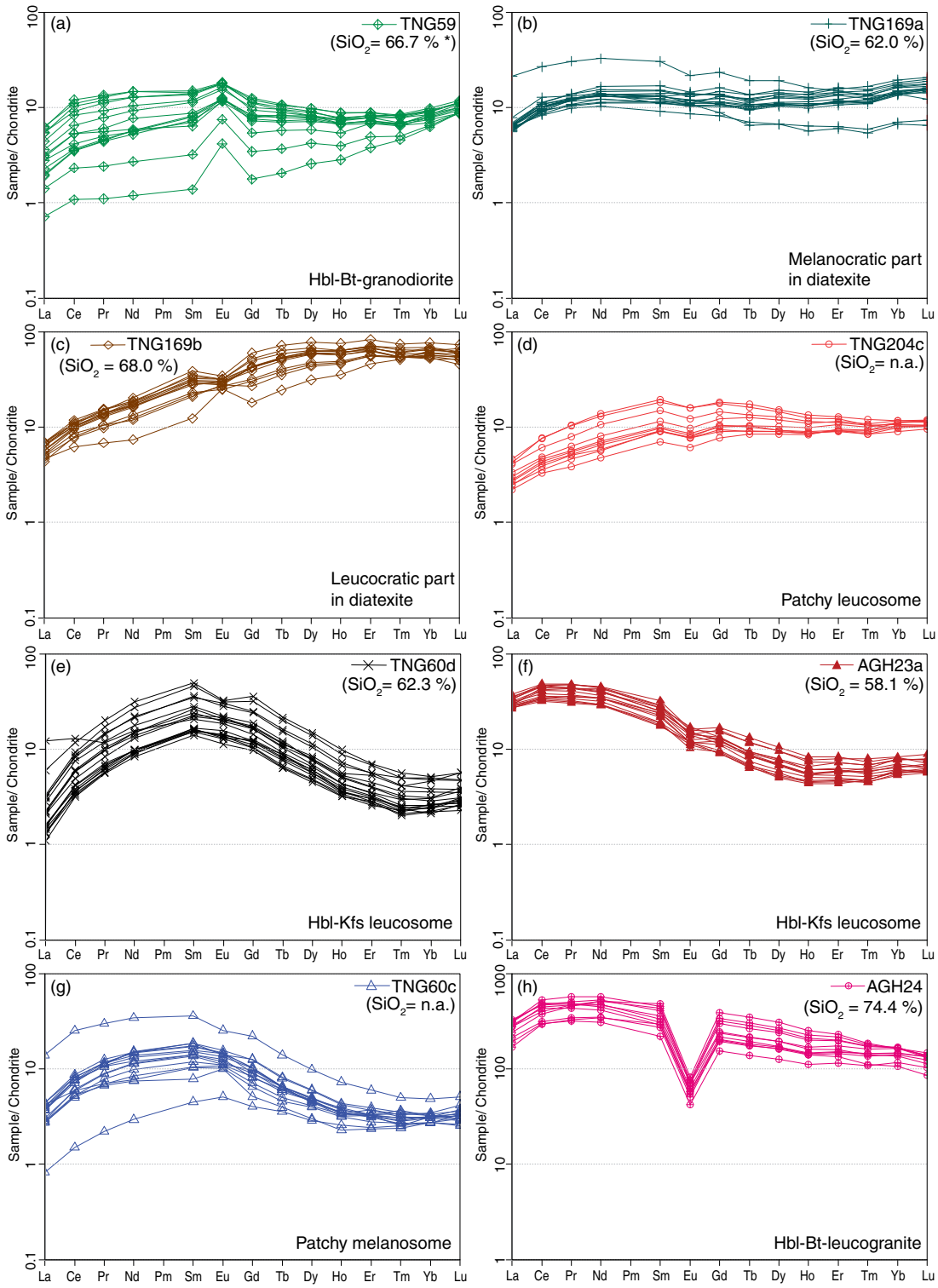

Fig. 13. Chondrite-normalized (Boynton, 1984) REE patterns for hornblende (Table 3). SiO_2 contents of whole-rock are indicated where available. *, Silica content for sample TNG59 is estimated from a comparable Hbl–Bt-granodiorite (sample TNG98a, Table 1). [Note different scale on the *y*-axis in (h).] Complete dataset is given in Supplementary Data Appendix 4.

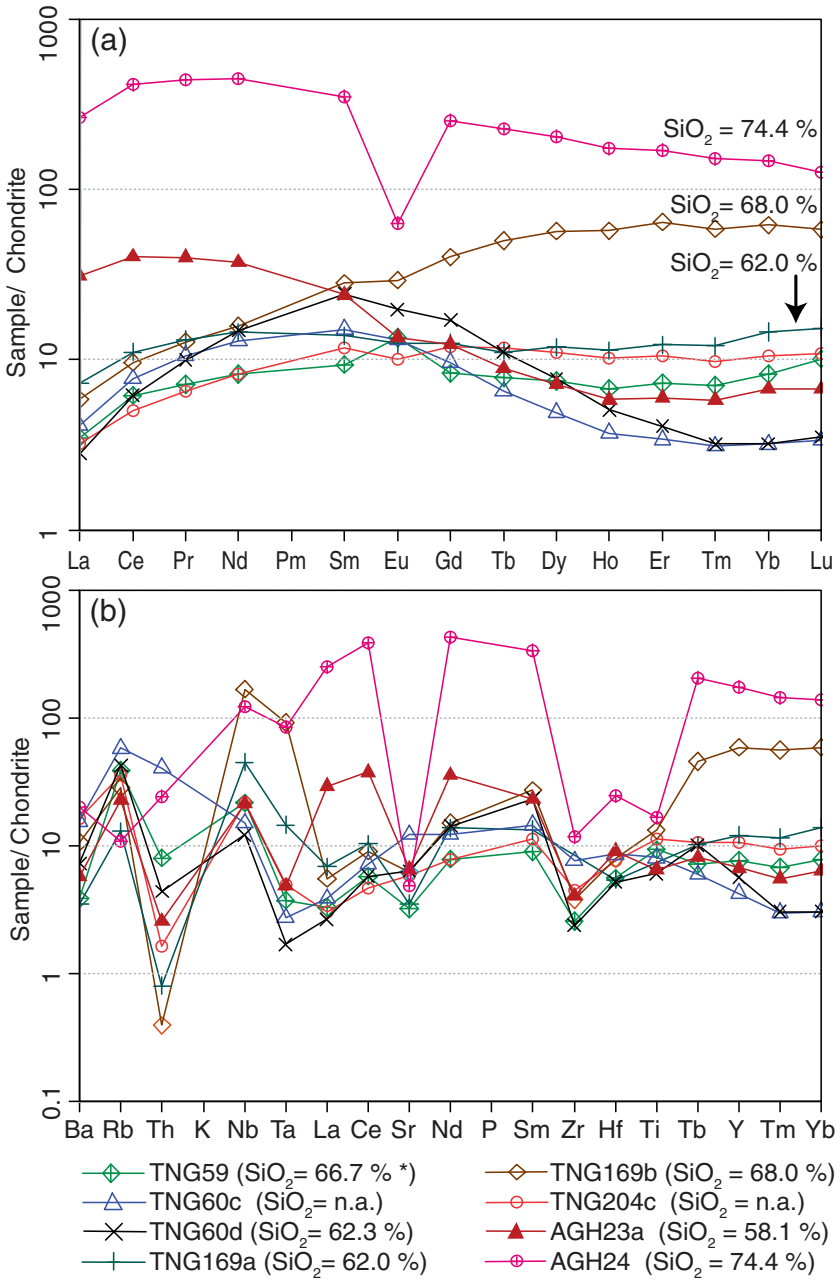

Fig. 14. (a) Chondrite-normalized (Boynton, 1984) REE patterns based on averages of hornblende analyses for all samples in Fig. 13. *, estimated value as in Fig. 13a. (b) Multi-element patterns of hornblende normalized to values of Sun & McDonough (1989).

each element modelled. The exact natures of the melting reactions are not part of the model. Thus, the results reflect only the bulk composition of the model melt.

Hornblendes in our leucosomes have unusual REE contents, and we therefore calculated their effective partition coefficients based on the ratio between REE in the grains and a whole-rock leucosome that we consider approximates the likely melt composition. This approach has two inherent dangers: (1) the analysed leucosome may not represent the melt composition; (2) the hornblende crystals may not have equilibrated with the melt. To minimize the risks in (1), we used the Hbl-free leucosome TNG113g as a typical melt composition (Table 1), because it has moderate Ba and Sr contents compared with the other leucosomes, and no Eu anomaly, suggesting that no significant loss of feldspar has occurred.

Table 3: Trace elements concentrations (ppm) of hornblende

Sample:	TNG59	TNG169a	TNG169b	TNG204c	TNG60c	TNG60d	AGH23a	AGH24
Rock type:	Hbl-Bt-granodiorite	melanocratic diatexite	leucocratic diatexite	leucosome	melanosome in diorite	Hbl-Kfs leucosome	Hbl-Kfs leucosome	Hbl-Bt-leucogranite
Average of *n* analyses:	*n* = 14	*n* = 17	*n* = 13	*n* = 10	*n* = 15	*n* = 18	*n* = 15	*n* = 11
Sc	72 ± 7	n.a.	115 ± 12	73 ± 9	31 ± 5	45 ± 6	43 ± 4	154 ± 42
Ti	5785 ± 256	n.a.	8224 ± 494	7042 ± 239	4997 ± 175	3742 ± 236	4047 ± 665	10297 ± 2109
V	443 ± 34	n.a.	274 ± 15	511 ± 76	357 ± 23	290 ± 22	262 ± 32	578 ± 150
Cr	133 ± 107	n.a.	32 ± 7	138 ± 25	28 ± 39	257 ± 183	82 ± 27	50 ± 12
Mn	4216 ± 131	3447 ± 380	5300 ± 211	2888 ± 64	2597 ± 148	3034 ± 169	3296 ± 151	4008 ± 793
Co	50 ± 2	n.a.	33 ± 1	53 ± 2	57 ± 4	61 ± 4	58 ± 4	47 ± 5
Ni	42 ± 5	n.a.	18 ± 1	116 ± 13	13 ± 2	152 ± 18	84 ± 17	11 ± 3
Cu	5 ± 5	n.a.	b.d	2 ± 1	11 ± 18	14 ± 17	6 ± 6	1 ± 1
Zn	366 ± 37	n.a.	460 ± 41	400 ± 20	570 ± 47	501 ± 26	502 ± 30	297 ± 29
Ga	37 ± 2	n.a.	40 ± 1	39 ± 2	39 ± 2	42 ± 2	26 ± 4	25 ± 3
Rb	14 ± 5	5 ± 1	10 ± 1	12 ± 1	20 ± 2	15 ± 1	8 ± 5	4 ± 1
Sr	38 ± 8	41 ± 6	73 ± 7	69 ± 5	145 ± 13	75 ± 6	77 ± 9	57 ± 14
Y	15 ± 3	24 ± 6	118 ± 19	21 ± 4	8 ± 2	11 ± 4	13 ± 3	350 ± 79
Zr	18 ± 2	n.a.	26 ± 3	30 ± 4	52 ± 91	16 ± 1	27 ± 4	80 ± 15
Nb	8 ± 1	16 ± 5	59 ± 7	8 ± 2	5 ± 1	4 ± 1	7 ± 2	43 ± 9
Ba	26 ± 49	24 ± 11	74 ± 11	114 ± 23	108 ± 12	50 ± 5	40 ± 13	139 ± 68
La	1·1 ± 0·6	2·3 ± 1·1	1·8 ± 0·3	1·0 ± 0·3	1·3 ± 0·9	0·9 ± 0·8	9·7 ± 1·0	82·8 ± 16·9
Ce	5·0 ± 2·8	9·0 ± 3·4	7·8 ± 1·3	4·1 ± 1·3	6·2 ± 4·2	5·0 ± 2·4	32·7 ± 4·8	333·8 ± 65·5
Pr	0·9 ± 0·5	1·6 ± 0·6	1·6 ± 0·3	0·8 ± 0·3	1·3 ± 0·7	1·2 ± 0·5	4·9 ± 0·8	54·1 ± 9·8
Nd	4·9 ± 2·6	8·7 ± 3·0	9·5 ± 2·1	4·9 ± 1·9	7·7 ± 4·2	8·9 ± 4·1	22·4 ± 3·5	269·7 ± 51·1
Sm	1·8 ± 0·8	2·7 ± 0·9	5·5 ± 1·4	2·3 ± 0·8	2·9 ± 1·4	4·7 ± 2·1	4·7 ± 0·9	68·7 ± 16·5
Eu	1·0 ± 0·3	0·9 ± 0·2	2·2 ± 0·2	0·7 ± 0·3	1·0 ± 0·3	1·5 ± 0·5	1·0 ± 0·2	4·7 ± 0·9
Gd	2·2 ± 0·8	3·3 ± 0·9	10·4 ± 2·9	3·1 ± 1·0	2·5 ± 1·1	4·4 ± 2·0	3·2 ± 0·6	66·1 ± 18·8
Tb	0·4 ± 0·1	0·5 ± 0·1	2·4 ± 0·6	0·6 ± 0·1	0·3 ± 0·1	0·5 ± 0·2	0·4 ± 0·1	10·8 ± 3·1
Dy	2·4 ± 0·7	3·8 ± 1·0	18·4 ± 3·9	3·5 ± 0·8	1·6 ± 0·5	2·5 ± 1·0	2·3 ± 0·5	66·2 ± 17·9
Ho	0·5 ± 0·1	0·8 ± 0·2	4·1 ± 0·7	0·7 ± 0·1	0·3 ± 0·1	0·4 ± 0·1	0·4 ± 0·1	12·5 ± 3·1
Er	1·5 ± 0·3	2·6 ± 0·6	13·6 ± 1·9	2·2 ± 0·3	0·7 ± 0·2	0·9 ± 0·3	1·3 ± 0·3	35·9 ± 7·6
Tm	0·2 ± 0·0	0·4 ± 0·1	1·9 ± 0·2	0·3 ± 0·0	0·1 ± 0·0	0·1 ± 0·0	0·2 ± 0·0	4·9 ± 0·9
Yb	1·7 ± 0·2	3·1 ± 0·7	13·0 ± 1·4	2·2 ± 0·2	0·7 ± 0·1	0·7 ± 0·2	1·4 ± 0·2	30·9 ± 4·4
Lu	0·3 ± 0·0	0·5 ± 0·1	1·9 ± 0·2	0·3 ± 0·0	0·1 ± 0·0	0·1 ± 0·0	0·2 ± 0·0	4·1 ± 0·6
Hf	1·1 ± 0·1	1·1 ± 0·1	1·6 ± 0·3	1·5 ± 0·2	1·7 ± 1·8	1·0 ± 0·1	1·8 ± 0·5	4·9 ± 0·8
Ta	0·1 ± 0·0	0·3 ± 0·1	1·8 ± 0·5	0·1 ± 0·0	0·1 ± 0·0	0·0 ± 0·0	0·1 ± 0·0	1·7 ± 0·5
Pb	5·5 ± 1·3	1·7 ± 0·5	3·2 ± 0·2	5·7 ± 0·4	28·1 ± 64·5	6·7 ± 1·5	4·2 ± 1·0	4·3 ± 0·6
Th	0·3 ± 0·5	0·0 ± 0·1	0·0 ± 0·0	0·1 ± 0·0	1·7 ± 5·5	0·2 ± 0·2	0·1 ± 0·0	1·0 ± 0·2
U	0·1 ± 0·1	0·1 ± 0·2	0·1 ± 0·0	0·1 ± 0·0	0·5 ± 0·9	0·1 ± 0·0	0·1 ± 0·0	0·2 ± 0·1
La_n/Yb_n	0·4 ± 0·2	0·5 ± 0·3	0·1 ± 0·0	0·3 ± 0·1	1·2 ± 0·6	0·9 ± 0·8	4·7 ± 0·6	1·8 ± 0·2
La_n/Sm_n	0·4 ± 0·1	0·5 ± 0·1	0·2 ± 0·1	0·3 ± 0·0	0·3 ± 0·1	0·1 ± 0·1	1·3 ± 0·2	0·8 ± 0·2
Gd_n/Yb_n	1·0 ± 0·4	0·9 ± 0·3	0·7 ± 0·2	1·1 ± 0·3	3·0 ± 0·9	5·3 ± 1·0	1·8 ± 0·2	1·7 ± 0·4
Eu/Eu*	1·5 ± 0·4	1·0 ± 0·1	0·9 ± 0·3	0·8 ± 0·0	1·1 ± 0·2	1·0 ± 0·1	0·8 ± 0·1	0·2 ± 0·0
Sum REE	24 ± 9	40 ± 11	94 ± 16	27 ± 7	27 ± 14	32 ± 13	85 ± 12	1045 ± 190

±indicates 1 standard deviation. Complete analysis is given in Supplementary Data Appendix 4.

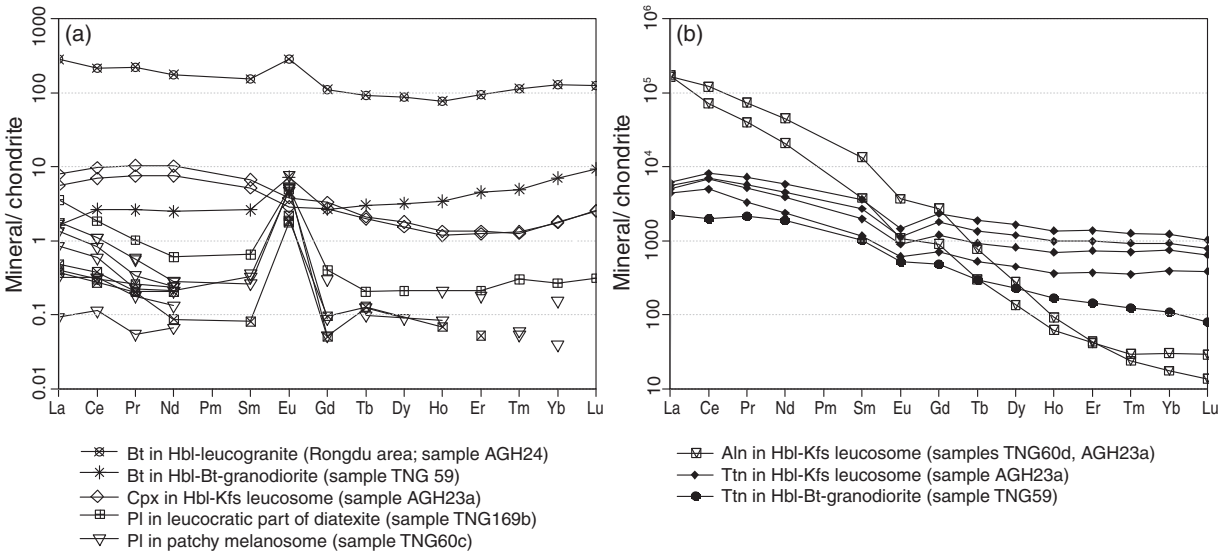

Fig. 15. (a) REE patterns of biotite, clinopyroxene and plagioclase. (b) REE patterns for allanite in Hbl–Kfs leucosome and titanite in Hbl–Bt-granodiorite and in Hbl–Kfs leucosome. Chondrite normalization after Boynton (1984). Analysis details are given in Supplementary Data Appendix 4.

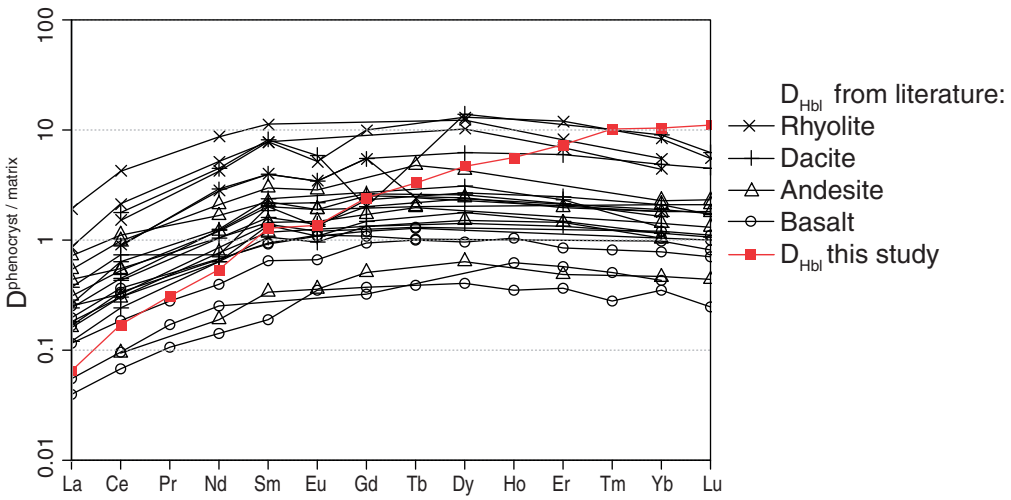

Fig. 16. Comparison of published partition coefficients for hornblende and calculated values from our own data. (Note large variations ranging from incompatibility to highly compatible in the data from the literature with rising values from basaltic to rhyolitic rocks.) Data taken from Higuchi & Nagasawa (1969; basalt), Nagasawa & Schnetzler (1971; dacite), Arth (1976; dacite), Arth & Barker (1976; dacite), Matsui *et al.* (1977; basalt, andesite), Dostal *et al.* (1983; basalt–andesite), Fujimaki *et al.* (1984; andesite), Luhr *et al.* (1984; trachyandesite), Bacon & Druitt (1988; andesite, rhyolite), Dalpe & Baker (1994; basanite–basalt), Sisson (1994; basalt–andesite, dacite, rhyolite), LaTourette *et al.* (1995; basanite), Klein *et al.* (1997; dacite), Botazzi *et al.* (1999; basalt) and Tiepolo *et al.* (2000; dacite).

Leucosomes with positive Eu anomalies and overall low REE contents (samples TNG170, TNG171, Fig. 7d) are most probably feldspar cumulates and are not used in the modelling. It is assumed that all hornblende is peritectic and that it has equilibrated with a melt equivalent to the leucosome in TNG113g. To minimize the risk of disequilibrium, we used hornblende that is subhedral, poikilitically encloses plagioclase and quartz, is compositionally homogeneous throughout the grain, and shares straight boundaries with plagioclase and quartz grains (hornblende in sample TNG204c in Tables 2 and 3).

Crystal/melt partition coefficients $D^{S/L}$ for hornblende were calculated using

$$D_i^{S/L} = \frac{C_i^S}{C_i^L}$$

where C^S is the concentration of element i in the solid (crystal), and C^L its concentration in the melt (with the composition of sample TNG113g, Table 1). Partition

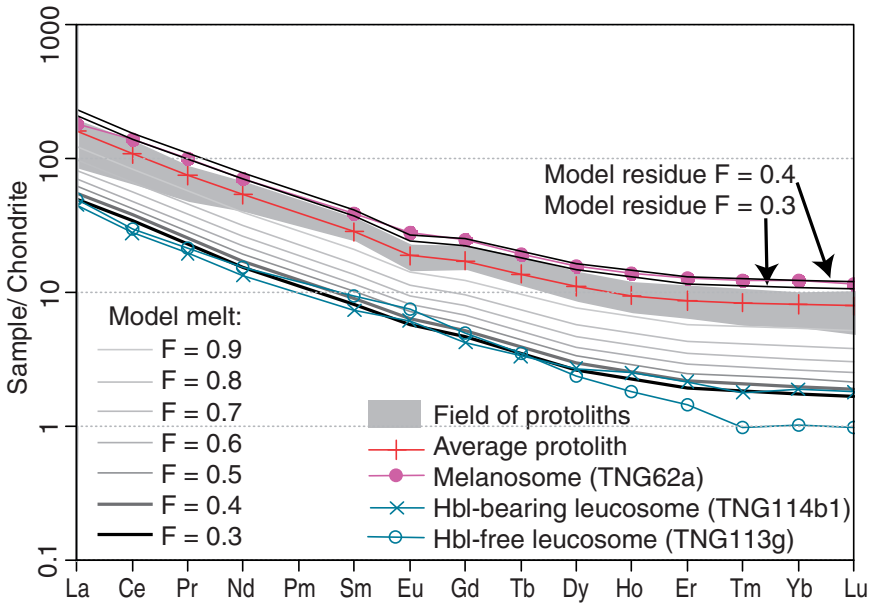

Fig. 17. Equilibrium batch melting models after Shaw (1970). The set of partition coefficients used is given in Table 4. Results show melt composition for 10% increments of partial melting. Representative Hbl-bearing leucosome is sample TNG114b1 (Table 1). Representative Hbl-free leucosome is sample TNG113g (Table 1). Partial melting of average ($n = 4$) Hbl–Bt-granodiorite protoliths (samples TNG98a, TNG207; Table 1) and diorite protoliths (samples TNG205a, TNG205b; Table 1). Grey field shows only limited variation in REE patterns of Hbl–Bt granodiorites and diorites. The model residue represents moderate partial melting of the protoliths. Mineral proportions of the model residue are expressed as fractions. Pl = 0·35, Kfs = 0·05, Qtz = 0·075, Hbl = 0·25, Bt = 0·25, Ttn = 0·015, Aln = 0·004, Ap = 0·004, Zrn = 0·002. These values are visual estimates only, based on thin sections.

Table 4: Partition coefficients used in batch melt model

Mineral	K_D La	K_D Ce	K_D Nd	K_D Sm	K_D Eu	K_D Gd	K_D Dy	K_D Er	K_D Yb	K_D Lu	Author(s)
Plagioclase	0.26*	0.24	0.17	0.13	2.11	0.9	0.09	0.08	0.08	0.06	Schnetzler & Philpotts (1970)
K-feldspar		0.04	0.03	0.02	1.13	0.01	0.01	0.06	0	0.006*	Schnetzler & Philpotts (1970)
Quartz	0.02	0.01	0.02	0.02	0.06	0.01	0.02	0.01	0.02	0.01	Nash & Crecraft (1985)
Hornblende	0.06	0.17	0.54	1.27	1.35	2.41	4.68	7.29	10.33	11.12	$D^{S/L}$ calculated as below
Biotite		0.04	0.04	0.06	0.15	0.08	0.1	0.16	0.18		Schnetzler & Philpotts (1970)
Titanite	46	87	152	204	181	200*	206	180*	104	92	Luhr & Carmichael (1980)
Zircon	1.14	1.17	1.38	2.03	0.85	6.01	44.9	107	516	689	Fujimaki (1986)
Apatite	28.2	29.6	57.1	84.8	9.22	100*	246	275	232	199	Nagasawa (1970)
Allanite	820	635	463	205	81	130	50	20	8.9	7.7	Brooks *et al.* (1981)
*interpolated values											
$D^{S/L}$ calculated from:											
Hbl crystal (ppm)	0.99	4.07	4.95	2.31	0.74	3.11	3.54	2.21	2.21	0.35	Hbl from sample TNG204c
Melt (ppm)	15.40	24.15	9.22	1.82	0.55	1.29	0.76	0.30	0.21	0.03	leucosome TNG113g

coefficient values derived in this manner are effective partition coefficients that result from the complexities of the melting reactions and melt–crystal equilibration involved in the migmatites studied here. They are not meant to be generalized partition coefficients. The calculated D values for REE in hornblende in comparison with published values are shown in Fig. 16.

We modelled partial melting of a representative calc-alkaline protolith with the composition of the average of the Hbl–Bt-granodiorites and quartz-diorites ($n = 4$).

Partial melting of the protolith was performed in 10% increments (Fig. 17). Melt derived from anatexis of the metasedimentary sequence is not included in the models, and neither is garnet as it is lacking in migmatites derived from calc-alkaline rocks. Small amounts of garnet are contained in Bt-psammites and pelites and are physically unrelated to the leucosomes in the rocks described here.

The mineral proportions in the model residue are based on visual estimates from thin sections of likely protoliths and a representative melanosome (TNG62a), and were chosen to reflect moderate partial melting of the protoliths; that is, to concur with observations in hand specimen and thin section. Accessory phases are included in the model because of their high influence on whole-rock REE distributions (Gromet & Silver, 1983; Bea, 1996). Estimating correctly the amount of accessory phases is fraught with difficulties. Their heterogeneous distribution and wide spacing between grains in our samples, particularly for allanite, makes point counting unreliable. Our estimates are thus a significant source of error in the models. Partition coefficients used in the models are given in Table 4.

To test if our model residue concurs with observations in nature, we calculated the batch melting residue using mass balance:

$$C^i_{RS} = \frac{C^i_0 - FC^i_L}{1 - F}.$$

The results in Fig. 17 show that for melt fractions between 30% and 40% ($F = 0{\cdot}3$ and $0{\cdot}4$, respectively), there is good agreement between the calculated melt compositions and a representative Hbl-bearing leucosome (sample TNG114b1). The REE patterns of melt residues for moderate amounts of partial melting ($F = 0{\cdot}3$ and $0{\cdot}4$) compare well with a representative melanosome (sample TNG62a), supporting the model estimates.

However, Hbl-free leucosomes have significantly lower HREE than the model melts above, and below we aim to reproduce this signature. Only few commonly occurring minerals are enriched in, and can fractionate HREE. These are cordierite, zircon, garnet and hornblende (Arth & Barker, 1976; Gromet & Silver, 1983; Bea *et al.*, 1994; Ayres & Harris, 1997). Cordierite and garnet were not found in our samples. Zircon fractionation is unlikely to be one of the major influences on the REE patterns because Zr contents are low in all rock types in our study and the Zr content of all the major rock types involved in anatexis is not too different (Zr average of protoliths, melanosomes, melanocratic diatexites = 147 ppm; Zr average for leucosomes, leucocratic diatexites = 104 ppm, Table 1). In contrast, hornblende is a rock-forming mineral in protoliths, melanosomes and leucosomes. Because we inferred from field observations that leucosomes with and without hornblende are linked in magma extraction networks at outcrop scale, we model the impact of retention of hornblende in migmatites on the trends towards Hbl-free leucosomes.

Hornblende retention

To simulate removal of hornblende from Hbl-bearing leucosomes, we subtract the REE contents of hornblende. This subtraction reflects purely mechanical filtering with known and fixed REE contents. Although this model is a rough approximation of the complex processes in nature into which we have only limited insight, the results can be used to establish a link between the chemistries of Hbl-bearing and Hbl-free leucosomes. Figure 18 compares the normalized REE patterns of hornblende from three samples: the Hbl-bearing leucosome sample TNG204c and a melanocratic and leucocratic part of the same diatexite (samples TNG169a and TNG169b, respectively), with the REE patterns of two Hbl-free leucosomes. Comparison between the REE patterns of hornblende and those of the Hbl-free leucosomes indicates their complementary nature: as contents increase in hornblende from LREE to HREE they decrease in the Hbl-free leucosomes.

We only have hornblende and whole-rock analyses of the melanocratic–leucocratic diatexite sample pair (TNG169a, TNG169b), and we use one of these samples in the model below. In Fig. 19, hornblende with the average REE composition from sample TNG169b (Table 3) is subtracted in 2% increments from the REE contents of the whole-rock diatexite sample TNG169b (Table 1), which has an estimated hornblende modal content of *c.* 10%. Removal of 6% hornblende results in a REE pattern subparallel to that of a representative Hbl-free leucosome (sample TNG113g used above as a melt representative) but with a higher total REE content. Removal of hornblende from the melanocratic part of the same diatexite (sample TNG169a) is not considered, because this sample is inferred to be a residual rock, in which hornblende and accessory phases have accumulated. However, removal of any of the hornblende types in Fig. 18 from a rock will have essentially the same effect, a systematic HREE depletion and thus increase of La_n/Yb_n values.

DISCUSSION

REE patterns of hornblende and partition coefficients

Hornblende in migmatites of the Karakoram Shear Zone shows large variations in REE contents, giving rise to different patterns in normalized trace element diagrams (Fig. 13). Despite a plethora of partition coefficients for hornblende being available, they do not explain the REE patterns in the hornblendes from this study. In general, the partition coefficients of REE in hornblende increase with decreasing ionic radius from the LREE to the MREE, reaching a maximum at Dy or Ho, and then slightly decrease towards the HREE, giving rise to an

overall concave-downward bell shape (e.g. Klein *et al.*, 1997; Bottazzi *et al.*, 1999). The compilation of hornblende partition coefficients in Fig. 16 shows that although the $D^{S/L}$ curves are subparallel, the values change by an order of magnitude as a function of the silica content and temperature of the melt, increasing from basaltic to granitic melts (e.g. Nagasawa & Schnetzler, 1971; Adam *et al.*, 1993; Hilyard *et al.*, 2000). Sisson (1994) showed increasing curvature of the REE patterns and a strong increase in HREE partitioning into hornblende when the magma approaches a rhyolitic composition.

The calculated apparent $D^{S/L}$ values for hornblende in this study are significantly different from those in the literature (Fig. 16). They show a continuous increase from the MREE to the HREE, and have significantly lower values for La/Yb or La/Lu. The hornblendes of the calc-alkaline Hbl–Bt-granodiorite protolith (sample TNG59, Fig 13a) are interpreted as crystals that equilibrated with a melt with ~65 wt % SiO_2. The REE patterns are relatively flat in comparison with hornblende patterns from melanosomes and leucosomes, and show positive Eu anomalies. Reported partition coefficients for Eu range from slight incompatibility to slight compatibility, but are always lower than those for the neighbouring element Gd [see data compilation of Tiepolo *et al.* (2007)], so that positive Eu anomalies should not be expected. Only negative Eu anomalies in hornblende have been reported and have been attributed to co-crystallization of plagioclase (Marks *et al.*, 2004). If this relationship holds true, negative Eu anomalies for hornblende would be expected to coincide with negative Sr anomalies because of the high partition coefficient for Sr in plagioclase.

Slight negative Eu and Sr anomalies were found for hornblende in a patchy tonalitic leucosome (Fig. 13d sample TNG204c), in which a hypidiomorphic magmatic texture is interpreted to represent equilibrium crystallization of hornblende with a melt phase (Fig. 4c and d). Hornblende in this leucosome (sample TNG204c) has REE patterns comparable with those from the Hbl–Bt-granodiorite protolith (sample TNG59, compare Fig. 13a and d) for the LREE to MREE but with slight enrichment in HREE, from Gd to Yb. This enrichment is interpreted to be the result of equilibration with a melt that has a higher silica content than the protolith.

The most pronounced difference between hornblende in different parts of a diatexite is shown in Fig 13b and c. Hornblende in the leucocratic part (Fig. 13c) shows strong enrichment in MREE to HREE compared with the melanocratic part (Fig. 13b). This difference may be the result of local equilibration with different phases in the migmatite. If so, hornblende in the melanocratic part may have equilibrated with restite phases such as titanite, which would result in MREE depletion in the hornblende. One interpretation for the high HREE concentrations in hornblende in the leucocratic part of the diatexite in Fig. 13c is equilibration with HREE-rich melt. We acknowledge this possibility but argue instead that this is a result of high hornblende HREE partition coefficient values, and that it is more likely that the hornblende grains equilibrated with a melt with a low HREE content, compositionally similar to the representative leucosome TNG113g.

Hornblende in Hbl–Kfs leucosomes (Fig. 13e and f, samples TNG60d, AGH23a) and in the diffuse melanosome (Fig. 13g, sample TNG60c) has distinct REE patterns and must have equilibrated under different conditions. The Hbl–Kfs leucosome in Fig. 13f (Rongdu location) contains hornblende with exceptionally high LREE concentrations. Allanite inclusions are common in these hornblende grains, and we speculate that volume diffusion between allanite and hornblende could have led to LREE enrichment in the hornblende. We emphasize, however, that it is unlikely that micro-inclusions were ablated during the analytical session, because high La and Ce values would have been coupled with high Th values, which was not the case. The REE patterns of hornblende grains from leucosome and melanosome (samples TNG60d and c, respectively, Fig. 13e and g) have similar shapes, but the leucosome shows stronger curvature and slight overall REE enrichment compared with the melanosome.

Based on petrographic observations, we conclude that the Hbl–Kfs leucosomes (Fig. 3c and d) are unlikely to represent crystallized melts, but are instead residual mineral assemblages left behind by an escaped melt. It is thus likely that their hornblende equilibrated with an already highly fractionated melt. A comparable interpretation was reached by Tiepolo *et al.* (2008) for hornblendes with differing REE content, from rocks that had been infiltrated by melts of different compositions. However, microprobe line analyses of large, poikilitic hornblende grains in the Hbl–Kfs leucosome reveal a relatively constant major element composition. The high contents of allanite, apatite and titanite in the Hbl–Kfs leucosomes seem to control the whole-rock REE contents (Table 1), and the unusual hornblende REE patterns suggest that they are also influenced by these accessory phases.

Hornblende in a leucogranite from the Karakoram Batholith at the Rongdu location (AGH24) has the highest total REE concentrations, and REE patterns that are distinct from those discussed above (Fig. 13h). Hornblende in this sample is also peculiar in that although the trace element concentrations, including REE, are comparable between single LA-ICP-MS spot analyses, the major element concentrations are highly variable (Figs 9 and 10). Commonly, these grains are extensively altered to biotite and white mica, and have irregular patchy zoning with

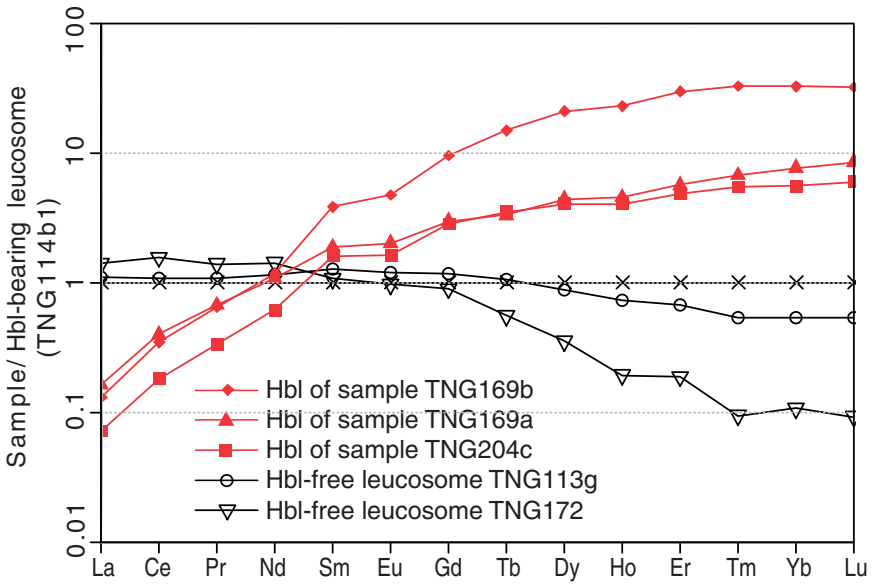

Fig. 18. REE patterns of hornblende grains and of whole-rocks, normalized to a representative Hbl-bearing leucosome, marked with cross symbols (sample TNG114b1). Hornblendes are depleted in LREE and enriched in HREE compared with the whole-rock. Hbl-free leucosomes are depleted in HREE and slightly enriched in LREE, a pattern explained by the removal of hornblende.

some grains having brown cores and green rims. Microprobe line analysis (Fig. 11) showed that the green rims have lower Al_{tot} contents compared with the cores. Because of these peculiarities, hornblende from this rock is not included in our petrogenetic considerations.

In summary, it is likely that the hornblende REE patterns determined here do not reflect the partition coefficients *sensu stricto*, but reflect local chemical environments, resulting from a complex history of equilibration with their surroundings during melting and crystallization, leading to effective partition coefficients. We postulate that absolute partition coefficients are generally not applicable to hornblendes found in rocks with complex melting and crystallization histories, such as migmatites. For these rocks, effective partition coefficients need to be determined, and this has considerable implications for modelling magmatic differentiation.

Role of hornblende in magma formation

We have documented partial melting of hornblende-bearing calc-alkaline arc rocks under water-fluxed conditions, giving rise to migmatites with peritectic hornblende. In the anatectic region, hornblende-rich restitic rocks form melanosomes in metatexites and diatexites. Commonly, leucosomes contain hornblende, and these are continuously linked with Hbl-free leucotonalitic to leucogranitic leucosomes with biotite as the main mafic mineral. These in turn feed into a network of magma escape pathways, linking to stocks and plutons (Weinberg *et al.*, 2009; Reichardt *et al.*, 2010). The leucogranite plutons in the Pangong Metamorphic Complex (PMC) are relatively free of xenoliths and generally do not contain hornblende. We thus infer that filtering must have taken place leaving hornblende and blocks of migmatites in the source.

Gradational changes, especially in the REE patterns, between protoliths, migmatites and the leucogranitic magmatic products (Fig. 7), correlate with different amounts of entrained restitic or newly formed hornblende. We thus interpret that, with the exception of the Hbl–Kfs leucosomes whose composition seems to be controlled by accessory minerals, hornblende is the major mineral controlling the REE patterns in the rocks documented here (Fig. 18).

Restitic schlieren are composed mostly of hornblende, biotite and titanite. Biotite has a negligible effect on the bulk-rock REE patterns as it has low partition coefficients for REE (e.g. Gromet & Silver, 1983). In contrast, titanite has high REE concentrations. However, because of its preference for MREE, significant titanite fractionation or accumulation would result in MREE depletion or enrichment, respectively, and this effect is not observed. Thus, we focus on hornblende, because it constitutes up to ~50 modal % in the melanosomes. Hbl–Bt-granodiorite and quartz-diorite protoliths show large compositional variations in the modal content of Hbl, between <10 and ~30 modal %. Our trace element data have shown that hornblende contains significant amounts of REE and is thus a major contributor to the whole-rock REE budget (Fig. 13). We have also discussed how hornblende REE partition coefficients from the literature do not explain the REE patterns observed and have therefore calculated our own effective partition coefficients (Table 4) used in the batch melting model presented. We note, however, that the

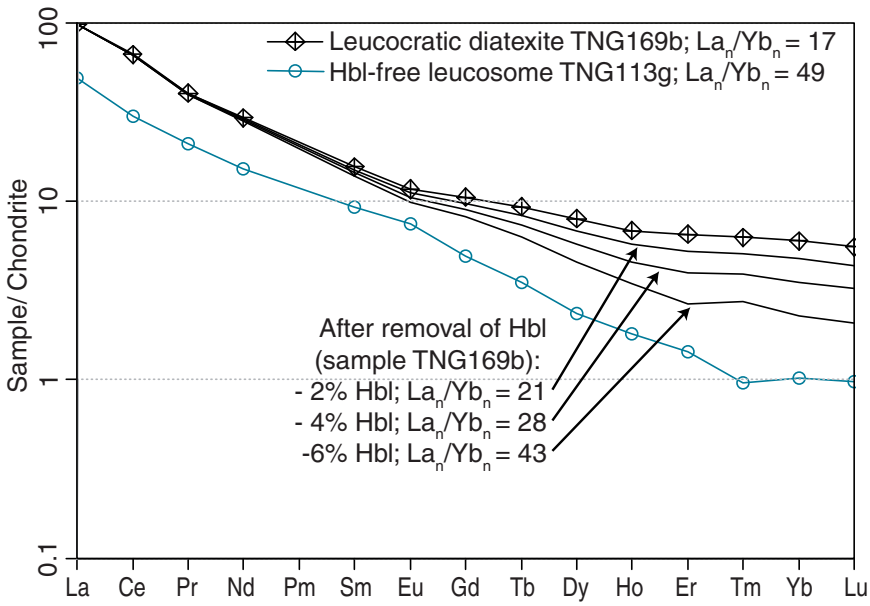

Fig. 19. Model for hornblende removal in 2% increments. Subtraction of hornblende analysed *in situ* in a thick section of the leucocratic diatexite TNG169b from the whole-rock composition of the same sample. Note progressive increase of La_n/Yb_n values that approach those of the Hbl-free leucosome.

measured REE contents of hornblende may not be the result of equilibration with a melt, whose composition we can only infer, but that they may also be influenced by co-crystallizing or restitic phases. Nevertheless, we assumed in our model that the hornblende in sample TNG204c grew in equilibrium with a melt compositionally similar to the leucosome sample TNG113g.

The hornblende subtraction model demonstrates that retention of hornblende in the source systematically increases La_n/Yb_n values (Fig. 19). We stress that the results of our model are not to be taken as absolute quantitative values, but can explain, qualitatively, the geochemical signatures. The resulting high La_n/Yb_n ratios are in agreement with the experiments of Tiepolo *et al.* (2000), who modelled hornblende fractionation for magmas ranging compositionally from mafic (<45 wt % SiO_2) to felsic (>60 wt % SiO_2).

Adakite and TTG signatures

The high La_n/Yb_n and Sr/Y values observed for leucogranites in the PMC (Fig. 6) are the most prominent features of adakites (Martin, 1987, 1999; Defant & Drummond, 1990; Martin *et al.*, 2005; Moyen, 2009). However, not every rock with high La_n/Yb_n and Sr/Y is an adakite. Adakites also have to be andesitic to dacitic in their bulk-rock composition, have $K_2O/Na_2O \leq 0{\cdot}42$ and generally show $Al_2O_3 > 15$ wt %, mg# ~50, Ni and Cr concentrations with average values of 24 and 36 ppm, respectively, and Y and Yb concentrations lower than 18 and 1·9 ppm, respectively (see Moyen, 2009). The leucogranites and diatexites in the PMC are not adakites based on the definition of Martin *et al.* (2005), because they are too silica-rich, have lower mg#, lower Cr and Ni contents, and generally have $K_2O/Na_2O > 0{\cdot}42$.

The high La_n/Yb_n and Sr/Y ratios of rocks in the PMC are comparable with values reported for granites of the Karakoram Batholith by Mahéo *et al.* (2009), and also with those for rocks from the Late Cretaceous Gangdese Batholith in South Tibet (Wen *et al.*, 2008) and Miocene granites in South Tibet (Xu *et al.*, 2010). However, like our leucogranites, these rocks also have mg# < 50 and lower Cr and Ni concentrations than adakites. Rocks with such signatures are sometimes referred to as pseudo-adakites (e.g. Wen *et al.*, 2008; Kamei *et al.*, 2009). In the interpretation of Wen *et al.* (2008), the most likely source rocks are older, calk-alkaline granitoids of the Gangdese Batholith, which is part of the Transhimalayan Batholith that includes the Ladakh arc (Honegger *et al.*, 1982; Schärer *et al.*, 1984; Weinberg & Dunlap, 2000) that borders the PMC in the region studied here. In the example of the Miocene granites of South Tibet, high La_n/Yb_n and Sr/Y values have been inferred to be the result of melting of Indian crust with minor contamination from other sources. All these rocks have been interpreted to be the result of partial melting of the lower crust, leaving behind residual hornblende and garnet (Wen *et al.*, 2008; Mahéo *et al.*, 2009; Xu *et al.*, 2010).

Based on the calculated effective $D^{S/L}$ values for hornblende, we demonstrate that for the example of the PMC leucogranites, hornblende is the main phase controlling

the HREE, and suggest that their 'pseudo-adakitic' or TTG-like signatures result from water-fluxed melting, associated with peritectic hornblende and its accumulation in the source at mid-crustal levels.

Nehring *et al.* (2009) modelled melting of amphibolite to generate magmas with an Archean TTG signature. Similar to adakites, these rocks require amphibole and garnet in the residue. In contrast, Tiepolo & Tribuzio (2008) suggested that hornblende fractionation may lead to cumulates in the source, giving rise to magmas with low HREE abundances and the concave-upward MREE to HREE pattern typical of TTGs. Our results echo those of Kamei *et al.* (2009), who modelled partial melting of arc-related tonalites and granodiorites with retainment of residual amphibole, and reproduced the high La_n/Yb_n and Sr/Y signature of granites in their study area.

Although a number of petrogenetic processes and geodynamic regimes can generate rocks with high La_n/Yb_n and Sr/Y values, Moyen (2009) concluded that, in general terms, melting of mafic rocks at great depths leaving residual amphibole and garnet in the source is responsible for the origin of the adakite- and TTG-like signature. In the exposures of anatectic middle crust in the PMC, the relations between protoliths, their migmatized equivalents and magmatic products can be directly studied, and removal of hornblende that has been produced by water-fluxed melting generates high La_n/Yb_n and Sr/Y signatures in the resultant melts, associated with other geochemical features that differentiate them from adakites and TTGs.

CONCLUSIONS

Metatexites and diatexites in the Pangong Metamorphic Complex associated with the Karakoram Batholith in Ladakh, NW India, resulted from water-fluxed partial melting of calc-alkaline plutonic rocks, giving rise to hornblende-bearing leucosomes. These leucosomes connect to a network of dykes that form magma escape pathways and link to Hbl-free leucogranite stocks and plutons (Weinberg *et al.*, 2009; Reichardt *et al.*, 2010), whereas hornblende forms residual cumulates that remain in the migmatitic source region. We have documented highly variable REE patterns for hornblende in protolith and migmatite samples, and derived effective REE partition coefficients for hornblende from a representative sample. We interpret the REE patterns and partition coefficients as resulting from a complex history of equilibration related to melting and crystallization processes during migmatite evolution. Our results demonstrate that retention of hornblende in the source, with no garnet involvement, may lead to leucogranites with high La_n/Yb_n and Sr/Y values.

ACKNOWLEDGEMENTS

We would like to thank Massimo Tiepolo for comments on an early version of the paper. We thank Ron Frost for his editorial work, and Calvin Barnes, Calvin Miller and Jonathan Miller for detailed constructive reviews that significantly helped to improve the paper. We also thank Massimo Raveggi for discussions on geochemistry.

FUNDING

This work was supported by funding from Australian Research Council Discovery Project DP0556409: The Early Stages of Granite Evolution: Extraction and Transport Through Ductile Crust.

SUPPLEMENTARY DATA

Supplementary data for this paper are available at *Journal of Petrology* online.

REFERENCES

Adam, J., Green, T. H. & Sie, S. H. (1993). Proton microprobe determined partitioning of Rb, Sr, Ba, Y, Zr, Nb and Ta between experimentally produced amphiboles and silicate melts with variable F content. *Chemical Geology* **109**, 29–49.

Arth, J. G. (1976). Behavior of trace elements during magmatic processes; a summary of theoretical models and their applications. *Journal of Research of the US Geological Survey* **4**, 41–47.

Arth, J. G. & Barker, F. (1976). Rare-earth partitioning between hornblende and dacitic liquid and implications for the genesis of trondhjemitic–tonalitic magmas. *Geology* **4**, 534–536.

Ayres, M. & Harris, N. (1997). REE fractionation and Nd-isotope disequilibrium during crustal anatexis: constraints from Himalayan leucogranites. *Chemical Geology* **139**, 249–269.

Bacon, C. R. & Druitt, T. H. (1988). Compositional evolution of the zoned calcalkaline magma chamber of Mount Mazama, Crater Lake, Oregon. *Contributions to Mineralogy and Petrology* **98**, 224–256.

Bea, F. (1996). Residence of REE, Y, Th and U in granites and crustal protoliths; implications for the chemistry of crustal melts. *Journal of Petrology* **37**, 521–552.

Bea, F., Pereira, M. D. & Stroh, A. (1994). Mineral/leucosome trace-element partitioning in a peraluminous migmatite (a laser ablation-ICP-MS study). *Chemical Geology* **117**, 291–312.

Bottazzi, P., Tiepolo, M., Vannucci, R., Zanetti, A., Brumm, R., Foley, S. F. & Oberti, R. (1999). Distinct site preferences for heavy and light REE in amphibole and the prediction of $^{Amph/L}D_{REE}$ partition coefficients for rare earth elements between amphibole and liquid. *Contributions to Mineralogy and Petrology* **137**, 36–45.

Bowen, N. L. (1919). Crystallization differentiation in igneous magmas. *Journal of Geology* **27**, 393–430.

Boynton, W. V. (1984). Cosmochemistry of the rare earth elements; meteorite studies. In: Henderson, P. (ed.) *Rare Earth Element Geochemistry. Developments in Geochemistry* **2**, 63–114.

Brooks, C. K., Henderson, P. & Roensbo, J. G. (1981). Rare-earth partition between allanite and glass in the obsidian of Sandy Braes, Northern Ireland. *Mineralogical Magazine* **44**, 157–160.

Dalpe, C. & Baker, D. R. (1994). Partition coefficients for rare-earth elements between calcic amphibole and Ti-rich basanitic glass at 1.5 Gpa, 1100 °C. In: Harte, B. (ed.) *V.M. Goldschmidt Conference.*

Edinburgh, United Kingdom: Mineralogical Society, London, United Kingdom, pp. 207–208.

Davidson, J., Turner, S., Handley, H., Macpherson, C. & Dosseto, A. (2007). Amphibole 'sponge' in arc crust? *Geology* **35**, 787–790.

Debon, F., Le Fort, P., Dautel, D., Sonet, J. & Zimmermann, J. L. (1987). Granites of western Karakorum and northern Kohistan (Pakistan): A composite mid-Cretaceous to upper Cenozoic magmatism. *Lithos* **20**, 19–40.

Defant, M. J. & Drummond, M. S. (1990). Derivation of some modern arc magmas by melting of young subducted lithosphere. *Nature* **347**, 662–665.

Defant, M. J., Xu, J. F., Kepezhinskas, P., Wang, Q., Zhang, Q. & Xiao, L. (2002). Adakites: Some variations on a theme. *Acta Petrologica Sinica* **18**, 129–142.

Dostal, J., Dupuy, C., Carron, J. P., Le Guen de Kerneizon, M. & Maury, R. C. (1983). Partition coefficients of trace elements; application to volcanic rocks of St. Vincent, West Indies. *Geochimica et Cosmochimica Acta* **47**, 525–533.

Drummond, M. S. & Defant, M. J. (1990). A model for trondhjemite–tonalite–dacite genesis and crustal growth via slab melting: Archean to modern comparisons. *Journal of Geophysical Research* **95**, 21503–21521.

Eggins, S. M., Woodhead, J. D., Kinsley, L. P. J., Mortimer, G. E., Sylvester, P., McCulloch, M. T., Hergt, J. M. & Handler, M. R. (1997). A simple method for the precise determination of ≥ 40 trace elements in geological samples by ICPMS using enriched isotope internal standardisation. *Chemical Geology* **134**, 311–326.

Femenias, O., Mercier, J.-C. C., Nkono, C., Diot, H., Berza, T., Tatu, M. & Demaiffe, D. (2006). Calcic amphibole growth and compositions in calc-alkaline magmas; evidence from the Motru dike swarm (Southern Carpathians, Romania). *American Mineralogist* **91**, 73–81.

Foley, S., Tiepolo, M. & Vannucci, R. (2002). Growth of early continental crust controlled by melting of amphibolite in subduction zones. *Nature* **417**, 837–840.

Frost, B. R., Barnes, C. G., Collins, W. J., Arculus, R. J., Ellis, D. J. & Frost, C. D. (2001). A geochemical classification for granitic rocks. *Journal of Petrology* **42**, 2033–2048.

Fujimaki, H. (1986). Partition coefficients of Hf, Zr, and REE between zircon, apatite, and liquid. *Contributions to Mineralogy and Petrology* **94**, 42–45.

Fujimaki, H., Tatsumoto, M. & Aoki, K.-I. (1984). Partition coefficients of Hf, Zr, and REE between phenocrysts and groundmasses. *Journal of Geophysical Research* **89**, 662–672.

Gardien, V., Thompson, A. B. & Ulmer, P. (2000). Melting of biotite + plagioclase + quartz gneisses; the role of H_2O in the stability of amphibole. *Journal of Petrology* **41**, 651–666.

Gromet, L. P. & Silver, L. T. (1983). Rare earth element distributions among minerals in a granodiorite and their petrogenetic implications. *Geochimica et Cosmochimica Acta* **47**, 925–939.

Gupta, L. N. & Johannes, W. (1982). Petrogenesis of a stromatic migmatite (Nelaug, southern Norway). *Journal of Petrology* **23**, 548–567.

Hammarstrom, J. M. & Zen, E. (1986). Aluminum in hornblende: an empirical igneous geobarometer. *American Mineralogist* **71**, 1297–1313.

Hermann, J. (2002). Allanite: thorium and light rare earth element carrier in subducted crust. *Chemical Geology* **192**, 289–306.

Higuchi, H. & Nagasawa, H. (1969). Partition of trace elements between rock-forming minerals and the host volcanic rocks. *Earth and Planetary Science Letters* **7**, 281–287.

Hilyard, M., Nielsen, R. L., Beard, J. S., Patiño-Douce, A. & Blencoe, J. (2000). Experimental determination of the partitioning behavior of rare earth and high field strength elements between pargasitic amphibole and natural silicate melts. *Geochimica et Cosmochimica Acta* **64**, 1103–1120.

Holtz, F., Pichavant, M., Barbey, P. & Johannes, W. (1992). Effects of H_2O on liquidus phase relations in the haplogranite system at 2 and 5 kbar. *American Mineralogist* **77**, 1223–1241.

Honegger, K., Dietrich, V., Frank, W., Gansser, A., Thöni, M. & Trommsdorff, V. (1982). Magmatism and metamorphism in the Ladakh Himalayas (the Indus–Tsangpo suture zone). *Earth and Planetary Science Letters* **60**, 253–292.

Johannes, W., Ehlers, C., Kriegsman, L. M. & Mengel, K. (2003). The link between migmatites and S-type granites in the Turku area, southern Finland. *Lithos* **68**, 69–90.

Johnson, M. C. & Rutherford, M. J. (1989). Experimental calibration of the aluminum-in-hornblende geobarometer with application of Long Valley caldera (California) volcanic rocks. *Geology* **17**, 837–841.

Kamei, A., Miyake, Y., Owada, M. & Kimura, J. I. (2009). A pseudo adakite derived from partial melting of tonalitic to granodioritic crust, Kyushu, southwest Japan arc. *Lithos* **112**, 615–625.

Kenah, C. & Hollister, L. S. (1983). Anatexis in the Central Gneiss Complex. In: Atherton, M. P. & Gribble, C. D. (eds) *Migmatites, Melting, and Metamorphism*. Nantwich: Shiva, pp. 142–162.

Klein, M., Stosch, H. G. & Seck, H. A. (1997). Partitioning of high field-strength and rare-earth elements between amphibole and quartz-dioritic to tonalitic melts: an experimental study. *Chemical Geology* **138**, 257–271.

Kretz, R. (1983). Symbols for rock-forming minerals. *American Mineralogist* **68**, 277–279.

Lappin, A. R. & Hollister, L. S. (1980). Partial melting in the Central Gneiss Complex near Prince Rupert, British Columbia. *American Journal of Science* **280**, 518–545.

LaTourrette, T., Hervig, R. L. & Holloway, J. R. (1995). Trace element partitioning between amphibole, phlogopite, and basanite melt. *Earth and Planetary Science Letters* **135**, 13–30.

Leake, B. E., Woolley, A. R., Arps, C. E. S., Birch, W. D., Gilbert, M. C., Grice, J. D., Hawthorne, F. C., Kato, A., Kisch, H. J., Krivovichev, V. G., Linthout, K., Laird, J., Mandarino, J. A., Maresch, W. V., Nickel, E. H., Rock, N. M. S., Schumacher, J. C., Smith, D. C., Stephenson, N. C. N., Ungaretti, L., Whittaker, E. J. W. & Guo, Y. (1997). Nomenclature of amphiboles; Report of the Subcommittee on Amphiboles of the International Mineralogical Association, Commission on New Minerals and Mineral Names. *American Mineralogist* **82**, 1019–1037.

Luhr, J. F. & Carmichael, I. S. E. (1980). The Colima Volcanic complex, Mexico—I. Post-caldera andesites from Volcan Colima. *Contributions to Mineralogy and Petrology* **71**, 343–372.

Luhr, J., Carmichael, I. S. E. & Varekamp, J. C. (1984). The 1982 eruptions of El Chichon Volcano, Chiapas, Mexico; mineralogy and petrology of the anhydrite-bearing pumices. *Journal of Volcanology and Geothermal Research* **23**, 69–108.

Mahéo, G., Blichert-Toft, J., Pin, C., Guillot, S. & Pêcher, A. (2009). Partial melting of mantle and crustal sources beneath south Karakorum, Pakistan: implications for the Miocene geodynamic evolution of the India–Asia Convergence Zone. *Journal of Petrology* **50**, 427–449.

Marchildon, N. & Brown, M. (2001). Melt segregation in late syn-tectonic anatectic migmatites: An example from the Onawa Contact Aureole, Maine, USA. *Physics and Chemistry of the Earth* **26**, 25–229.

Marks, M., Halama, R., Wenzel, T. & Markl, G. (2004). Trace element variations in clinopyroxene and amphibole from alkaline to peralkaline syenites and granites: implications for mineral–melt trace-element partitioning. *Chemical Geology* **211**, 185–215.

Martin, H. (1987). Petrogenesis of Archaean trondhjemites, tonalites, and granodiorites from eastern Finland: major and trace element geochemistry. *Journal of Petrology* **28**, 921–953.

Martin, H. (1994). The Archean grey gneisses and the genesis of continental crust. *Developments in Precambrian Geology* **11**, 205–259.

Martin, H. (1999). Adakitic magmas; modern analogues of Archaean granitoids. *Lithos* **46**, 411–429.

Martin, H., Smithies, R. H., Rapp, R., Moyen, J.-F. & Champion, D. (2005). An overview of adakite, tonalite–trondhjemite–granodiorite (TTG), and sanukitoid; relationships and some implications for crustal evolution. *Lithos* **79**, 1–24.

Matsui, Y., Onuma, N., Nagasawa, H., Higuchi, H. & Banno, S. (1977). Crystal structure control in trace element partition between crystal and magma. *Bulletin de la Société Française de Minéralogie et de Cristallographie* **100**, 315–324.

McCarthy, M. R. & Weinberg, R. F. (2010). Structural complexity resulting from pervasive ductile deformation in the Karakoram Shear Zone, Ladakh, NW India. *Tectonics* **29**, 18, doi:10.1029/2008TC002354.

McLellan, E. L. (1988). Migmatite structures in the Central Gneiss Complex, Boca de Quadra, Alaska. *Journal of Metamorphic Geology* **6**, 517–542.

Mehnert, K. R. (1968). *Migmatites and the Origin of Granitic Rocks*. Amsterdam, London, New York: Elsevier Publishing Corporation, p. 393.

Moyen, J.-F. (2009). High Sr/Y and La/Yb ratios: The meaning of the 'adakitic signature'. *Lithos* **112**, 556–574.

Nagasawa, H. (1970). Rare earth concentrations in zircons and apatites and their host dacites and granites. *Earth and Planetary Science Letters* **9**, 359–364.

Nagasawa, H. & Schnetzler, C. C. (1971). Partitioning of rare earth, alkali and alkaline earth elements between phenocrysts and acidic igneous magma. *Geochimica et Cosmochimica Acta* **35**, 953–968.

Nash, W. P. & Crecraft, H. R. (1985). Partition coefficients for trace elements in silicic magmas. *Geochimica et Cosmochimica Acta* **49**, 2309–2322.

Nehring, F., Foley, S. F., Holtta, P. & Van Den Kerkhof, A. M. (2009). Internal differentiation of the Archean continental crust: fluid-controlled partial melting of granulites and TTG–amphibolite associations in central Finland. *Journal of Petrology* **50**, 3–35.

Patiño Douce, A. E. (1999). What do experiments tell us about the relative contributions of crust and mantle to the origin of granitic magmas?. In: Castro, A., Fernandez, C. & Vigneresse, J.-L. (eds) *Understanding Granites. Integrating New and Classical Techniques. Geological Society, Volume 168.* London: Special Publications, pp. 55–75.

Patiño Douce, A. E. & Harris, N. (1998). Experimental constraints on Himalayan anatexis. *Journal of Petrology* **39**, 689–710.

Petford, N. & Atherton, M. (1996). Na-rich partial melts from newly underplated basaltic crust; the Cordillera Blanca Batholith, Peru. *Journal of Petrology* **37**, 1491–1521.

Phillips, R. J., Parrish, R. R. & Searle, M. P. (2004). Age constraints on ductile deformation and long-term slip rates along the Karakoram fault zone, Ladakh. *Earth and Planetary Science Letters* **226**, 305–319.

Ravikant, V. (2006). Utility of Rb–Sr geochronology in constraining Miocene and Cretaceous events in the eastern Karakoram, Ladakh, India. *Journal of Asian Earth Sciences* **27**, 534–543.

Ravikant, V., Wu, F.-Y. & Ji, W.-Q. (2009). Zircon U–Pb and Hf isotopic constraints on petrogenesis of the Cretaceous–Tertiary granites in eastern Karakoram and Ladakh, India. *Lithos* **110**, 153–166.

Reichardt, H. & Weinberg, R. F. (2012). The dike swarm of the Karakoram shear zone, Ladakh, NW India: Linking granite source to batholith. *Geological Society of America Bulletin* **124**(1–2), 89–103.

Reichardt, H., Weinberg, R. F., Andersson, U. B. & Fanning, C. M. (2010). Hybridization of granitic magmas in the source: The origin of the Karakoram Batholith, Ladakh, NW India. *Lithos* **116**, 249–272.

Rolland, Y. & Pêcher, A. (2001). The Pangong granulites of the Karakoram Fault (western Tibet); vertical extrusion within a lithosphere-scale fault? *Comptes Rendus de l'Académie des Sciences, Série II* **332**, 363–370.

Rolland, Y., Picard, C., Pêcher, A., Lapierre, H., Bosch, D. & Keller, F. (2002). The Cretaceous Ladakh arc of NW Himalaya—slab melting and melt–mantle interaction during fast northward drift of Indian Plate. *Chemical Geology* **182**, 139–178.

Rolland, Y., Mahéo, G., Pêcher, A. & Villa, I. M. (2009). Syn-kinematic emplacement of the Pangong metamorphic and magmatic complex along the Karakorum Fault (N Ladakh). *Journal of Asian Earth Sciences* **34**, 10–25.

Sawyer, E. W. (1999). Criteria for the recognition of partial melting. In: Brown, M. G. & Kotkova, J. (eds) *Crust melting in nature and experiment, Volume 24*. Oxford: Pergamon, Oxford, International, pp. 269–279.

Sawyer, E. W. (2001). Melt segregation in the continental crust: distribution and movement of melt in anatectic rocks. *Journal of Metamorphic Geology* **19**, 291–309.

Schärer, U., Hamet, J. & Allègre, C. J. (1984). The Transhimalaya (Gangdese) plutonism in the Ladakh region: a U–Pb and Rb–Sr study. *Earth and Planetary Science Letters* **67**, 327–339.

Schmidt, M. W. (1992). Amphibole composition in tonalite as a function of pressure; an experimental calibration of the Al-in-hornblende barometer. *Contributions to Mineralogy and Petrology* **110**, 304–310.

Schnetzler, C. C. & Philpotts, J. A. (1970). Partition coefficients of rare-earth elements between igneous matrix material and rock-forming mineral phenocrysts—II. *Geochimica et Cosmochimica Acta* **34**, 331–340.

Searle, M. P., Weinberg, R. F. & Dunlap, W. J. (1998). Transpressional tectonics along the Karakoram Fault Zone, northern Ladakh. In: Holdsworth, R. E., Strachan, R. A. & Dewey, J. F. (eds) *Continental Transpressional and Transtensional Tectonics. Geological Society, Volume 135.* London: Special Publications, pp. 307–326.

Shaw, D. M. (1970). Trace element fractionation during anatexis. *Geochimica et Cosmochimica Acta* **34**, 237–243.

Singh, S., Kumar, R., Barley, M. E. & Jain, A. K. (2007). SHRIMP U–Pb ages and depth of emplacement of Ladakh Batholith, Eastern Ladakh, India. *Journal of Asian Earth Sciences* **30**, 490–503.

Sisson, T. W. (1994). Hornblende–melt trace-element partitioning measured by ion microprobe. *Chemical Geology* **117**, 331–344.

Spear, F. S. (1981). An experimental study of hornblende stability and compositional variability in amphibolite. *American Journal of Science* **281**, 697–734.

Sun, S. S. & McDonough, W. F. (1989). Chemical and isotopic systematics of oceanic basalts; implications for mantle composition and processes. In: Saunders, A. D. & Norry, M. J. (eds) *Magmatism in the Ocean Basins. Geological Society, Volume 42.* London: Special Publications, pp. 313–345.

Tiepolo, M. & Tribuzio, R. (2008). Petrology and U–Pb zircon geochronology of amphibole-rich cumulates with sanukitic affinity from Husky Ridge (northern Victoria Land, Antarctica); insights into the role of amphibole in the petrogenesis of subduction-related magmas. *Journal of Petrology* **49**, 937–970.

Tiepolo, M., Vanucci, R., Bottazzi, P., Oberti, R., Zanetti, A. & Foley, S. (2000). Partitioning of rare earth elements, Y, Th, U, and

Pb between pargasite, kaersutite, and basanite to trachyte melts; implications for percolated and veined mantle. *Geochemistry, Geophysics, Geosystems - G3* **1**, 2000GC000064.

Tiepolo, M., Oberti, R., Zanetti, A., Vannucci, R. & Foley, S. F. (2007). Trace-element partitioning between amphibole and silicate melt. In: Hawthorne, F. C., Oberti, R., Della Ventura, G. & Mottana, A. (eds) *Amphiboles; crystal chemistry, occurence and health issues*. Washington, DC: Mineralogical Society of America and Geochemical Society, pp. 417–452.

Tulloch, A. J. & Kimbrough, D. L. (2003). Paired plutonic belts in convergent margins and the development of high Sr/Y magmatism: Peninsular Ranges Batholith of Baja California and Median Batholith of New Zealand. In: Johnson, S. E., Paterson, S. R., Fletcher, J. M., Girty, G. H., Kimbrough, D. L. & Martin-Barajas, A. (eds) *Tectonic evolution of northwestern Mexico and the southwestern USA*. Boulder, CO: Geological Society of America, pp. 275–295.

Upadhyay, R., Frisch, W. & Siebel, W. (2008). Tectonic implications of new U–Pb zircon ages of the Ladakh Batholith, Indus suture zone, northwest Himalaya, India. *Terra Nova* **20**, 309–317.

van Achterbergh, E., Ryan, C. G., Jackson, S. E. & Griffin, W. L. (2001). Data reduction software for LA-ICP-MS. In: Sylvester, P. J. (ed.) *Short Course Handbook*. Ottawa, ON, Canada: Mineralogical Association of Canada, pp. 239–243.

Weinberg, R. F. & Dunlap, W. J. (2000). Growth and deformation of the Ladakh Batholith, Northwest Himalayas; implications for timing of continental collision and origin of calc-alkaline batholiths. *Journal of Geology* **108**, 303–320.

Weinberg, R. F. & Mark, G. (2008). Magma migration, folding, and disaggregation of migmatites in the Karakoram shear zone, Ladakh, NW India. *Geological Society of America Bulletin* **120**, 994–1009.

Weinberg, R. F. & Searle, M. P. (1998). The Pangong Injection Complex, Indian Karakoram: a case of pervasive granite flow through hot viscous crust. *Journal of the Geological Society, London* **155**, 883–891.

Weinberg, R. F., Dunlap, W. J. & Whitehouse, M. (2000). New field, structural and geochronological data from the Shyok and Nubra valleys, northern Ladakh: linking Kohistan to Tibet. In: Khan, M. A., Treloar, P. J., Searle, M. P. & Jan, M. Q. (eds) *Tectonics of the Nanga Parbat Syntaxis and the Western Himalaya. Geological Society, London, Special Publications* **170**, 253–275.

Weinberg, R. F., Mark, G. & Reichardt, H. (2009). Magma ponding in the Karakoram shear zone, Ladakh, NW India. *Geological Society of America Bulletin* **121**, 278–285.

Wen, D.-R., Chung, S.-L., Song, B., Iizuka, Y., Yang, H.-J., Ji, J., Liu, D. & Gallet, S. (2008). Late Cretaceous Gangdese intrusions of adakitic geochemical characteristics, SE Tibet: Petrogenesis and tectonic implications. *Lithos* **105**, 1–11.

Xu, W. C., Zhang, H. F., Guo, L. & Yuan, H. L. (2010). Miocene high Sr/Y magmatism, south Tibet: Product of partial melting of subducted Indian continental crust and its tectonic implication. *Lithos* **114**, 293–306.